


Review

A Critical Review of the Use of Bismuth Halide Perovskites for CO₂ Photoreduction: Stability Challenges and Strategies Implemented

Edith Luévano-Hipólito ¹, Oscar L. Quintero-Lizárraga ² and Leticia M. Torres-Martínez ^{2,3,*}

¹ Departamento de Ecomateriales y Energía, Facultad de Ingeniería Civil, Consejo Nacional de Ciencia y Tecnología—Universidad Autónoma de Nuevo León, Cd. Universitaria, San Nicolás de los Garza C.P. 66455, NL, Mexico

² Departamento de Ecomateriales y Energía, Facultad de Ingeniería Civil, Universidad Autónoma de Nuevo León, Cd. Universitaria, San Nicolás de los Garza C.P. 66455, NL, Mexico

³ Centro de Investigación en Materiales Avanzados, S. C. (CIMAV) Miguel de Cervantes 120 Complejo Ind. Chihuahua, Chihuahua 31136, CH, Mexico

* Correspondence: lettorresg@yahoo.com

Abstract: Inspired by natural photosynthesis, the photocatalytic CO₂ reduction reaction (CO₂RR) stands as a viable strategy for the production of solar fuels to mitigate the high dependence on highly polluting fossil fuels, as well as to decrease the CO₂ concentration in the atmosphere. The design of photocatalytic materials is crucial to ensure high efficiency of the CO₂RR process. So far, perovskite materials have shown high efficiency and selectivity in CO₂RR to generate different solar fuels. Particularly, bismuth halide perovskites have gained much attention due to their higher absorption coefficients, their more efficient charge transfer (compared to oxide perovskites), and their required thermodynamic potential for CO₂RR. Moreover, these materials represent a promising alternative to the highly polluting lead halide perovskites. However, despite all the remarkable advantages of bismuth halide perovskites, their use has been limited, owing to instability concerns. As a consequence, recent reports have offered solutions to obtain structures highly stable against oxygen, water, and light, promoting the formation of solar fuels with promising efficiency for CO₂RR. Thus, this review analyzes the current state of the art in this field, particularly studies about stability strategies from intrinsic and extrinsic standpoints. Lastly, we discuss the challenges and opportunities in designing stable bismuth halide perovskites, which open new opportunities for scaling up the CO₂RR.

Keywords: bismuth halide perovskites; stability strategies; CO₂ photoreduction; solar fuels; extrinsic approach; intrinsic approach



Citation: Luévano-Hipólito, E.; Quintero-Lizárraga, O.L.; Torres-Martínez, L.M. A Critical Review of the Use of Bismuth Halide Perovskites for CO₂ Photoreduction: Stability Challenges and Strategies Implemented. *Catalysts* **2022**, *12*, 1410. <https://doi.org/10.3390/catal12111410>

Academic Editors: Kai Yang and Changlin Yu

Received: 10 October 2022

Accepted: 3 November 2022

Published: 11 November 2022

Publisher's Note: MDPI stays neutral with regard to jurisdictional claims in published maps and institutional affiliations.



Copyright: © 2022 by the authors. Licensee MDPI, Basel, Switzerland. This article is an open access article distributed under the terms and conditions of the Creative Commons Attribution (CC BY) license (<https://creativecommons.org/licenses/by/4.0/>).

1. Introduction

The continuous increase in the concentration of CO₂ in the atmosphere is driven by the high global electricity demand, estimated at approximately 1400 Terawatt-hours per year [1]. In 2021, the CO₂ emissions derived from the energy sector were 36.3 Gt, the highest annual quantity ever registered, caused by the sudden rebound from the global pandemic lockdown in 2020 [2]. Therefore, the pollution related to the increased CO₂ concentration in the atmosphere continues to be a matter of concern that requires action and global decision making.

Several solutions have been proposed to mitigate the environmental impact of the high CO₂ concentration in the atmosphere. The efforts have been diverse, and there are certain approaches that stand out. For instance, the promulgation of environmental regulations focuses on carrying out preventive actions to avoid the emission of pollutants into the atmosphere. Another option to reduce CO₂ emissions is to improve the energy efficiency of the already-established fossil fuels, since this would result in a better use of these energetic resources [3,4]. Likewise, it is possible to use renewable fuels whose combustion reaction

generates products with a lower environmental impact, e.g., natural gas, methanol, biogas, or alternative energy sources that do not involve the use of fossil fuels. However, these fuels are commonly obtained through the use of nonrenewable and highly polluting fossil fuels. Alternatively, some technologies allow the use of CO₂ as a raw material in different processes in order to synthesize many industrial utility products (commodities) [5–9]. One of these processes is the production of short-chain hydrocarbons (solar fuels) through heterogeneous photocatalysis from CO₂ reduction [10–15]. This is one of the most promising technologies to help mitigate CO₂ pollution, since it can make use of sunlight to reduce CO₂, employing semiconductors and water. In this process, it is possible to capture and transform CO₂ into nonharmful products that, in some cases, can serve different purposes. However, the implementation of this technology at higher scales has been limited by the low efficiency of the photocatalysts. Nonetheless, materials with perovskite structure have been reported to exhibit an outstanding efficiency in CO₂RR. Thus, in this work, we discuss recent advancements, challenges, and improvement strategies using a family of compounds which have been little-explored despite their interesting properties: bismuth halide perovskites (A₃Bi₂X₉; ABi₃X₁₀, etc.; where A = monovalent cations and X = halogens). This review aims to propose innovative strategies to design promising materials for photocatalytic CO₂RR that could serve in helping close the gap in current efforts to reach global sustainability and reduce the excessive concentration of CO₂ in the atmosphere.

2. Photocatalytic CO₂ Reduction

The photocatalytic CO₂ reduction reaction (CO₂RR) is an attractive option due to the simplicity of the process, which requires CO₂, H₂O, and a photocatalyst as raw materials to generate solar fuels. These materials are introduced to a batch or continuous photocatalytic reactor with CO₂, H₂O, and in some cases, additional sacrificial agents. Then, the reactor is irradiated with natural or artificial sunlight to promote the formation of the electron (e[−]) and hole (h⁺) pair that reacts with the adsorbed chemical species (e.g., CO₂) on the catalyst surface, carrying out its reduction to different solar fuels. This process can generate a variety of C1 and C2 compounds with value on the market, such as formic acid (HCOOH), carbon monoxide (CO), formaldehyde (HCHO), methanol (CH₃OH), acetic acid (CH₃COOH), methane (CH₄), ethanol (C₂H₅OH), or ethane (C₂H₆), as shown in Figure 1 [10,15].

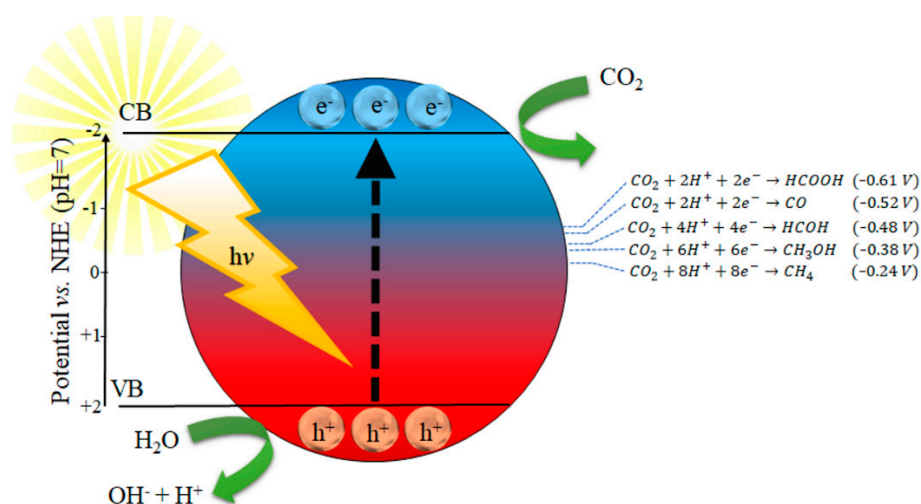


Figure 1. Schematic illustration of the photocatalytic CO₂ reduction to different solar fuels and their reduction potentials.

Among the aforementioned products, one that requires a lower thermodynamic potential for its formation is CH₄, while the production of CO and HCOOH both demand the lowest number of electrons, which can be easily generated by kinetic energy. However,

other factors can modulate the photocatalytic activity of material and the production of a specific solar fuel, among which the following stand out:

- The energy of photoexcitation. The energy and density of photons significantly affect the distribution of photoexcited electrons, resulting in different reaction mechanisms and influencing their C1 and C2 selectivity [16]. It has been shown that strong light reception of the material, higher photon energy, and high light intensity favor the generation of a higher number of electron–hole pairs during the photocatalytic CO₂ reduction.
- Band engineering. Engineering the band structure of photocatalysts allows for the modulation of reduction potentials in the semiconductor materials, which can influence the selectivity of a generated product. For this matter, doping is one of the simplest and most effective ways to modulate the band structure of photocatalysts, along with the use of heterojunctions, which harness the reduction potentials of various photocatalysts [17].
- Intermediate products. A weak interaction of the by-products with the photocatalyst will result in a faster desorption to the reaction medium. In this manner, the selectivity of the desired product could be modified through the nonintervention of by-products [18–20]. Previous work demonstrated that weak physical adsorption between CO and C promotes its desorption and improves the selectivity towards CO. On the other hand, a strong chemisorption between CO and N-containing groups on carbon can promote the photocatalytic CO₂ reduction to CH₄ [18].
- The separation of photogenerated charges. The density of photogenerated electrons on the surface of photocatalysts can influence surface reactions and affect the selectivity of a given generated product. This density mainly depends on the separation efficiency of photogenerated electrons and holes in the photocatalysts. This can be modulated with metal charging, heterojunctions, the adjustment of intrinsic charge carrier mobilities, and the construction of an internal electric field [21–23].
- CO₂ affinity. The CO₂ adsorption on the photocatalyst's surface significantly affects the reaction efficiency and product selectivity. The CO₂ molecule in the gas phase is an inert linear molecule with an ∠OCO angle of 180° and a length of C–O bonds close to 1.1 Å. Upon adsorption on photocatalysts, CO₂ is activated into negatively charged CO₂^{δ−} species, and the ∠OCO angle is decreased to 140°, while the length of C–O bonds is stretched up to 1.3 Å. CO₂^{δ−} is a key intermediate for producing carbon-containing products from photocatalytic CO₂ reduction [24]. Thus, CO₂ adsorption is one of the most critical steps during the photocatalytic reaction. Recent works suggest that the type of CO₂ binding on the photocatalyst's surface influenced the selectivity for the generation of CO, CH₄, CH₃OH, and HCOOH in continuous and batch reactors [25]. Moreover, studies show that the CO₂ affinity of the photocatalysts is promoted by favoring basic sites on their surface [26,27], N-functionalization [28], and oxygen vacancy engineering [25,29]. Likewise, it is possible to improve CO₂ adsorption by modifying the reaction conditions; for instance, lowering reaction temperature and increasing partial pressure [30].
- Surface area. Porous materials are superior candidates for enhancing the CO₂ adsorption on the photocatalysts' surfaces for their photocatalytic conversion, which is normally achieved by loading active components onto porous supports [31–33]. This property can influence the selectivity of the photocatalytic CO₂ reduction to obtain products of higher molecular weight. For example, the selectivity of the reaction for CH₃OH and HCOOH generation can be increased by supporting Cu₂O nanoparticles on porous materials [31]. At the beginning of the reaction, unidentate CO₂ species are adsorbed in bare and supported Cu₂O nanoparticles, which can be converted to the carboxyl radical (COOH●) under irradiation. Then, the carboxyl radical reacts with H⁺ to form HCOOH, which is dehydrated to HCO●. This intermediate is easily adsorbed on the photocatalyst surface, and it could determine the selectivity of the reaction. Lower surface areas promote an easier desorption of HCO●, favoring the formation of HCOH; meanwhile, higher surface areas can maintain this compound hydrogenated until the formation of CH₃OH.

3. Photocatalysts with Outstanding Performances for CO₂RR

Scaling CO₂RR at pilot and industrial levels requires the design of photocatalyst materials with outstanding efficiencies and stabilities over extended periods. Other requirements may include chemical stability, low toxicity, high CO₂ conversion efficiency, high surface area, cost-effectiveness, accessibility, resistance to photocorrosion, and adequate redox potential to generate different solar fuels [8,10,34].

Inoue et al. were the first research group to report the photocatalytic CO₂RR using different photocatalysts (e.g., TiO₂, WO₃, ZnO, CdS, GaP, and SiC) suspended under UV-Visible irradiation [35], generating HCOOH, HCOH, CH₃OH, and CH₄ as reaction products. Some of these photocatalysts are still used for CO₂ reduction; however, to obtain higher efficiencies, it is necessary to implement certain modifications. Some of these variations may include heterojunctions, anion functionalization, or encapsulation using porous materials [36–40].

Titanium dioxide (TiO₂) has been the most widely used photocatalyst since the earliest reports. It has many valuable properties: high photocatalytic activity, stability, inertness to chemical corrosion, and low toxicity. In addition, TiO₂ can perform CO₂RR to generate value-added products with good efficiencies, such as formic acid (HCOOH; 2954 μmol g⁻¹ h⁻¹) and formaldehyde (HCHO; 16,537 μmol g⁻¹ h⁻¹), under UV irradiation; however, to achieve these high efficiencies it was necessary to use high pressures (7–20 bar), a high temperature (80 °C), and Na₂SO₃ as a sacrificial agent [41].

Alternatively, other photocatalytic materials have also been utilized for CO₂RR with promising efficiencies. Some examples of these photocatalysts are scheelites AMO₄ (A = Ca, Sr, Ba) [42], AV₂O₆ (A = Ca, Sr, Ba) [43], rGO-CuO [44], Ti-MOF [45], Ni/BaTiO₃ [46], Cu/In₂O₃ [47], simple perovskites (ABO₃, A = Li, Na, K, B = Ta, Nb) [48,49], SrTiO₃ [50], LaCoO₃ [51], and recently, halide perovskites ABX₃ (A = formamidinium, FA, methylammonium, MA, or Cs; B = Pb, Bi, or Sn; and X = Cl, Br or I) [52]. The aforementioned materials have stood out because they exhibit remarkable properties for use in photocatalytic CO₂RR, such as:

- (i) Ease of synthesis. These materials are distinguished by their low enthalpy of formation, which often grants them facile synthesis processes at normal temperatures (~25 °C) and pressures (~1 atm). Also, it allows for the formation of different morphologies with a high number of active sites [53,54].
- (ii) Structure modulation. It has been demonstrated that perovskites can modulate their crystalline structures and energy bands by incorporating anions or cations from different groups [55–58]. In addition, the polarization refinement structure can induce an intensive internal electric field, which facilitates charge migration to the surface, improving the efficiency of CO₂RR [59]. On the other hand, the structure modulation can be carried out by variation of the morphology (e.g., bulk, nanoplates, nanorods, quantum dots, etc.) [60–62].
- (iii) Light harvesting. The modulation of the composition of a halide perovskite can significantly alter its band gap, which can make it an excellent light harvester compared with other semiconductors. At an atomic level, the most common strategies for light-harvesting enhancement include extending the absorption range via band gap engineering, applying the plasmonic resonance enhancement effect, and the arrangement of light absorption using tandem absorber devices [63]. Recently, Jian et al. have proposed the formation of CsPbBr₃ nanocrystals with O-defective WO₃ composites as a solution for stable and highly efficient materials that can harvest the broadest solar spectrum possible [64]. This strategy increases CO₂RR efficiency up to 7-fold compared to pristine materials.
- (iv) Exciton generation. The efficient generation of electron–hole pairs under excitation can enhance the photoconversion efficiency in CO₂RR and other applications, such as photovoltaics and photon detection [65]. This phenomenon is mainly seen in narrow-band perovskites, which can promote multiple exciton generation (MEG). Perovskite materials can exhibit a variety of exciton species under different excita-

tion conditions, including biexciton and triple exciton [66]. The surface defects of perovskite are the main source of the production of charged excitons. Under weak light excitation, this is mostly generated by single exciton recombination; meanwhile, at medium excitation intensity, biexciton recombination is favored. On the other hand, by using strong light excitation, Auger recombination dominates the generation of charged excitons, and perovskite materials are mainly characterized by their recombination of these excitons. Lin et al. demonstrated that the decay time of single excitons and biexcitons in Mn–CsPbBr₃ perovskites can be modified by applying an external magnetic field (300 mT), suppressing the recombination of the photogenerated charges and subsequently improving the efficiency of CO and CH₄ generation from CO₂RR [67].

- (v) Long carrier diffusion lengths. Long carrier lifetime makes halide perovskite materials high-performance photovoltaic materials. Chen et al. proposed that the band-edge carrier lifetime increases when the system transitions from a lower rotational entropy to another phase with higher entropy [68]. These results suggest that the recombination of the photogenerated pair is inhibited by screening, leading to the formation of polarons and thereby extending their lifetime.
- (vi) Band structure. Generally, perovskite materials have adequate redox potentials in their valence and conduction bands for CO₂RR. Figure 2 shows the band structures of selected perovskite-structured materials. The bands were calculated by Equations (1) and (2), considering the band gap (E_g) of each material, the absolute electronegativity (X), and the energy of free electrons (E^e) on the hydrogen scale (4.5 eV). In general, halide perovskites exhibited less negative conduction potentials than the simple perovskites; however, they have the thermodynamical potential required to reduce the CO₂ to different solar fuels.

$$E_{VB} = X - E^e + 0.5E_g \quad (1)$$

$$E_{CB} = X - E^e - 0.5E_g \quad (2)$$

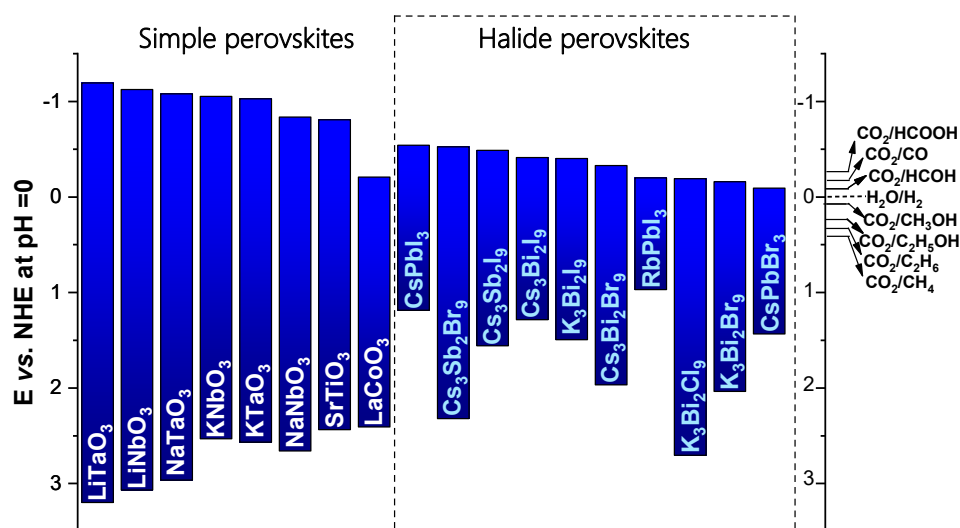


Figure 2. Band structure of some selected materials with perovskite structure.

4. Metal Halide Perovskites for CO₂RR

Perovskite materials exhibit several promising features that have recently brought attention to their field of study. Perovskite structures are isostructural configurations to calcium titanate (CaTiO₃; a mineral commonly found in nature) and other cation variations (e.g., Ta or Nb). The general formula of perovskite materials is ABX₃, where A stands for organic or inorganic cations (e.g., MA⁺, FA⁺, NH₄⁺, K⁺, Sr²⁺, Ca²⁺, etc.) having larger radii than B (e.g., Ti⁴⁺,

Bi^{3+} , Pb^{2+} , Ta^{4+} , Nb^{4+} , etc.) and X are anions, either oxides (O_2^-) or halogens (I^- , Br^- , Cl^- , or F^-) [69–71]. In these structures, the central atom is not in direct contact with its neighboring coordination atoms, commonly giving these compounds the rare property of ferroelectricity [72] and other promising optoelectronic characteristics. Additionally, the use of organic ions on the A- and X-sites of perovskites leads to several geometric and structural degrees of freedom, which allows for detailed studies on the composition–structure–property relations of these materials [73]. Hydrogen bonds commonly assemble amino groups and halide ions in hybrid organic–inorganic perovskite structures; in which case, their ionic bonding facilitates their synthesis at low temperatures [74].

There are several factors that bolster the photovoltaic properties of metal halide perovskites, such as their high symmetry, the periodicity of their crystal structure (commonly referred to as 1D, 2D, or 3D perovskites), the arrangement of their polar organic cations, the ionic energy of their halides' anions, and the electronic configuration of the B-site cation of their structure [75]. These characteristics also increase their likelihood to obtain high photocatalytic yields [76]. More specifically, lead halide perovskites (LHP) have shown outstanding efficiencies for CO_2 photoreduction [77], owing to their narrow band gaps and adequate band structure suitable for carrying out the photocatalytic CO_2RR . In addition, these materials have good charge transport properties [78], which allows charges to be efficiently separated and transferred within LHP band structure [79].

4.1. Lead Halide Perovskites (LHP)

The general formula of LHPs is APbX_3 , where A = organic and inorganic cations (e.g., Ca, K, Cs, Na, CH_3NH_3 , or $\text{CH}(\text{NH}_2)_2$) and X = halides (e.g., I, Br, Cl, or F). Inorganic cations are preferable, as they are more stable [80]. The unit cell of the APbX_3 crystal lattice usually has a cubic geometry in which the Pb^{2+} cation is in the center of the octahedra, coordinating with six X anions to form $[\text{BX}_6]^{4-}$ ions, while the A-site cation is located at the vertices.

CsPbBr_3 perovskites have a particularly high photocatalytic performance for CO_2 photoreduction [77,81,82]. The highest yield registered to date for this metal halide perovskite was described by Chen et al., who reported the generation of CO/CH_4 with efficiencies up to $1724 \mu\text{mol g}^{-1}$ under UV light [81]. Other authors have also reported the activity of this perovskite to produce CO from CO_2RR in heterojunctions with graphitic carbon nitride ($149 \mu\text{mol g}^{-1} \text{h}^{-1}$) [82], Bi_2WO_6 ($\text{CO}+\text{CH}_4$; $503 \mu\text{mol g}^{-1}$) [77], and MXene (CH_4 , $27 \mu\text{mol g}^{-1} \text{h}^{-1}$) [83]. Also, the CsPbBr_3 perovskite demonstrated high stability in 10 cycles of consecutive CO_2RR evaluation for CO/CH_4 generation [84].

4.2. Lead-Free Halide Perovskites (LFHP)

Despite the promising activity of LHPs, the presence of lead in their structure could generate environmental toxicity problems. Therefore, various efforts have been made to replace this metal without sacrificing its superior performance, leading to the development of lead-free halide perovskites (LFHP). One of the most frequent ones is the alteration of the periodicity in the crystalline arrangement of LHP materials, which is achieved by modifying their layers to optimize their optical properties [85]. For this purpose, different synthesis methods have been developed using various reactants, solvents, and ligands that allow for the obtention of desired optical properties in these materials and a high environmental stability [86]. As a result, many elements have been used to form various perovskite structures.

Different families of chemical elements can form LFHP structures, such as some transition metals (Pd [87], Cd [88]), chalcogenides (Zr, Hf) [89], and La [90]. There is great potential in replacing Pb with group 14 metals; however, Sn^{2+} and Ge^{2+} cations tend to undergo oxidation due to the high-energy 5s orbitals, which promotes a highly unstable structure at ambient exposure [91]. There are also reports on the use of mixed or trivalent cations to form structures of the $\text{A}_3\text{B}_2\text{X}_9$ or $\text{A}_2\text{B}^+\text{B}^{3+}\text{X}_6$ types. Alternatively, Bi^{3+} and Sb^{3+} ions are promising candidates to replace Pb^{2+} and develop stable, lead-free perovskites.

In some cases, these structures exhibit low-dimensional $A_3M(III)_2X_9$ structures whose properties have not been extensively studied, especially in photocatalytic CO₂RR.

The perovskite structures possess the general formula of ABX₃, as discussed above. The optical properties of the perovskite materials can be tuned by changing the A, B, or X ions present in the ABX₃ structure. The size of A, B, and X should satisfy the Goldschmidt tolerance factor (t), as shown in Equation (3):

$$t = \frac{r_A + r_X}{\sqrt{2}(r_B + r_x)} \quad (3)$$

In this equation, variables r_A , r_B , and r_X are the ionic radii of each element in the ABX₃ structure [92]. The perovskite materials show good stability when the tolerance factor is equal or close to 1. In the case of LFHPs, bismuth has a similar ionic radius to lead (as well as comparable properties), the tolerance factor rule is satisfied, and the stability of the Bi-based perovskite materials is enhanced when the substitution takes place. Moreover, it was found that Bi-based perovskite materials possess a higher absorption coefficient, which renders them an efficient light-absorbing material for solar cell applications and, recently, for photocatalytic applications [92–97]. This is supported by reports on the use of Cs₃Bi₂I₆Br₃ films as solar cells, for which the highest power conversion efficiency (PCE) reported so far was 1.15% [93]. In addition, bismuth halides have been demonstrated to be good candidates for oxidizing a variety of organic compounds, such as thiamazole [94], vanillyl alcohol [95], rhodamine B [96], phenol [97], etc.

5. Bismuth Halide Perovskites

Among the different options for replacing the Pb²⁺ cation, bismuth provides an attractive option due to its nontoxic nature and chemical stability [98]. Its trivalent (3+) oxidation state causes materials to form an $A_3Bi_2X_9$ structure, where A can be K⁺, Rb⁺, Cs⁺, or methylammonium MA⁺, and X can be I, Br, or Cl. Some of them have shown low toxicity, stability in air, and ease of synthesis [99]. In addition, as shown in Figure 2, this family has the required thermodynamic potentials to reduce CO₂ to different fuels, such as HCOOH, CO, CH₃OH, CH₄, C₂H₅OH, or C₂H₆, which positions bismuth halide perovskites as promising materials to carry out the photocatalytic CO₂RR.

5.1. Crystal Structure of the $A_3Bi_2X_9$ Family

The $A_3Bi_2X_9$ family of materials crystallize in different systems, depending on the halide anion used. For example, Cs₃Bi₂Cl₉ has a monoclinic unit cell; meanwhile, Cs₃Bi₂Br₉ and Cs₃Bi₂I₉ have hexagonal structures (Figure 3a) [100]. Particularly, the structure of Cs₃Bi₂I₉ is composed of bioctahedral (Bi₂I₉)^{3−} clusters surrounded by Cs cations, which are situated between these clusters in such a way that a nearly ideal hexagonal-type close packing of the cesium and iodine atoms takes place. Each layer in the close packing has the same configuration, with three iodide atoms for each Cs atom.

Figure 3b shows the structure of MA₃Bi₂I₉ for reference purposes. This structure has a hexagonal symmetry (P63/mmc) with face-sharing BiI₆ dioctahedral (Bi₂I₉)^{3−} clusters isolated by MA⁺. One MA⁺ group is surrounded by six metal halide octahedra [101]. Figure 3c shows the unit cell of the Rb₃Bi₂I₉, which contains corrugated layers of corner-connected BiI₆ octahedra [102]. The crystal structure of Rb₃Bi₂I₉ can be described as a distorted defect variant of the perovskite type (P21/n) in which only two-thirds of the octahedral sites are occupied. An ordered cubic close packing of Rb and I also occurs, where the BiI₆ octahedra are coordinated by eight Rb atoms in a distorted cube, the unit cell of the perovskite type. On the other hand, another set of perovskite materials can be formed using K⁺ as the A cation. The K₃Bi₂I₉ perovskite crystallizes in a monoclinic structure with a P21/n space group [103]. This forms a 2D-layered structure with distorted BiI₆ corner-sharing octahedra. However, there are no reports about its use in photocatalytic applications.

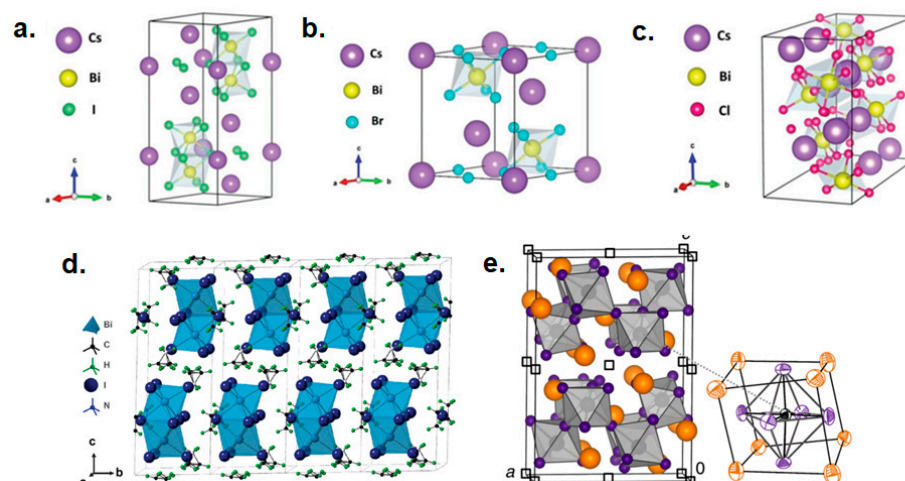


Figure 3. Crystal structure of the $A_3Bi_2X_9$ family: (a) $Cs_3Bi_2I_9$, (b) $Cs_3Bi_2Br_9$, (c) $Cs_3Bi_2Cl_9$, (d) $MA_3Bi_2Br_9$, and (e) $Rb_3Bi_2I_9$. Adapted from [100–102].

5.2. Performance of $A_3Bi_2X_9$ Family in CO₂RR

So far, most of the reports related to CO₂RR using this family employ Cs^+ as the A-site cation. Shen et al. reported the photocatalytic activity of quantum dots (QD) of the $Cs_3Bi_2X_9$ ($X=Cl, Br, \text{ and } I$) family from the perspective of surface engineering. They mainly studied the effect of the type of halogen associated with surface regulation [104]. The results showed that $Cs_3Bi_2Br_9$ displayed the highest activity for CO production ($135 \mu\text{mol g}^{-1}$), with 98.7% selectivity after 5 h of artificial solar light; meanwhile, $Cs_3Bi_2I_9$ exhibited poor activity, possibly due to its intrinsic instability under irradiation (Figure 4a). The highest activity of the $Cs_3Bi_2Br_9$ perovskite was attributed to a more efficient charge transfer with longer lifetimes, which often grants more free charges for CO₂RR, as shown in Figure 4b.

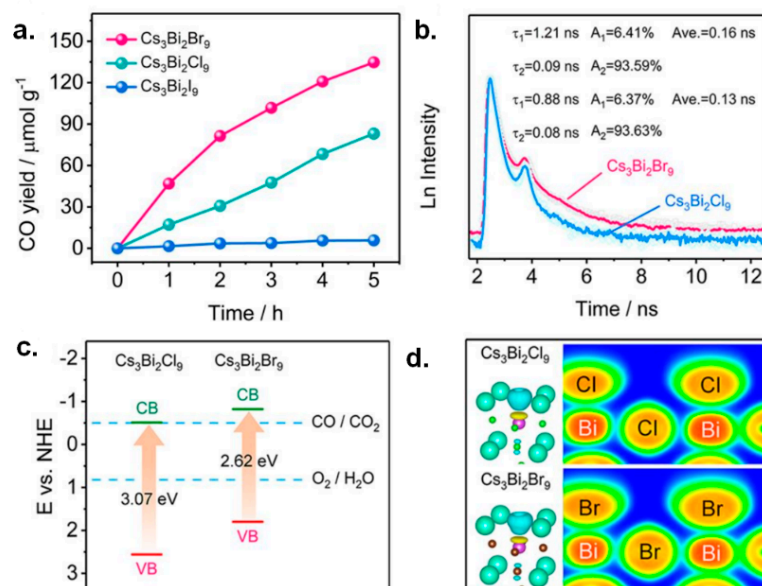


Figure 4. Investigation of the effect of different halogen ions in $Cs_3Bi_2X_9$ for CO production from CO₂RR: (a) Time-dependent CO production, (b) Time-resolved fluorescence emission decay spectra, (c) Band structure, and (d) Charge difference distributions and electronic location function of $Cs_3Bi_2Cl_9$ and $Cs_3Bi_2Br_9$. Adapted from [104].

Since band structures influence the reactivity of a photocatalyst, a more negative potential in CB would indicate a higher capacity for photogenerated electrons to reduce

CO₂ to different fuels. Figure 4c shows that both Cs₃Bi₂Br₉ and Cs₃Bi₂Cl₉ possess suitable bandgaps and adequate band-edge potentials to carry out the CO₂RR to CO. Remarkably, the band-edge positions exhibit a VB upshift with halogen substitution from Cl to Br, while there was little change on CB. These results confirm that the presence of Br in Cs₃Bi₂X₉ promoted an enhanced solar energy utilization and photoreduction capability due to its profitable electronic band structures. Moreover, the density functional theory (DFT) method was used to clarify the internal electron transfer direction change in using Br or Cl in the Cs₃Bi₂X₉ perovskite. As is shown in Figure 4d, Bi atoms are depleted, and X atoms are charge-accumulated, which reflects thicker electron cloud density in the Cs₃Bi₂Br₉ perovskite (mainly in the Br-site). Additionally, the authors demonstrated a higher CO₂ affinity in Cs₃Bi₂Br₉ than in the rest of the samples, according to the b-CO₃²⁻ signals obtained by FTIR. These results confirm that the selection of Br as the anion in the Cs₃Bi₂X₉ structure is the best pathway to design a new and more efficient photocatalyst for CO₂RR.

On the other hand, the effect of modifying the A-site with Rb⁺, Cs⁺, and CH₃NH₃⁺ (MA⁺) in the A₃Bi₂I₉ structure was investigated by Bhosale et al. [98]. The origin of the application of bismuth halide perovskites derives from the promising performance of Cs₃Bi₂I₉ and MA₃Bi₂I₉ in solar cells of 1.15% and 3.17%, respectively [93,105]. The A₃Bi₂I₉ (A = Rb, Cs, and MA) perovskites were synthesized by a top-down ultrasonic method that favored the formation of nanoparticles with diameters lower than 20 nm. Interestingly, Cs₃Bi₂I₉ and MA₃Bi₂I₉ perovskites crystallized in hexagonal structures of space group P63/mm; while the Rb₃Bi₂I₉ sample had a monoclinic system with space group P21/n. All the samples exhibited activity reducing the CO₂ to CO and CH₄. However, some differences were detected. For example, the highest efficiency for CH₄ production (17 μmol g⁻¹) was obtained with the Rb₃Bi₂I₉ perovskite; meanwhile, Cs₃Bi₂I₉ exhibited the highest selectivity for CO generation (77 μmol g⁻¹), which is one of the best results obtained in comparison with other perovskites under similar experimental conditions. The differences in the selectivity of both samples were attributed to the formation of monodentate and bridge carbonates in Rb₃Bi₂I₉ and Cs₃Bi₂I₉, respectively.

Electron Paramagnetic Resonance (EPR) demonstrated that in Rb₃Bi₂I₉ and Cs₃Bi₂I₉ samples, holes are efficiently stabilized with Bi⁴⁺ and oxygen ions; nonetheless, for MA₃Bi₂I₉, holes are additionally stabilized by •CH₂NH₃⁺. As a result, the transfer of h⁺ into water is less efficient in MA₃Bi₂I₉, resulting in a lower charge transfer efficiency. The crystal structure of the studied samples also influenced the efficiency of CO₂RR. Rb₃Bi₂I₉ crystallizes in a distorted defect variant of the perovskite structure in which every third Bi layer within the face [001] is depleted. Therefore, since Bi constitutes the active site of the catalyst, its depletion in Rb₃Bi₂I₉ favored lower CO₂RR efficiencies compared to Cs₃Bi₂I₉.

These works demonstrated the potential of the A₃Bi₂X₉ family to act as a photocatalyst in CO₂RR, showing efficiencies higher than other traditional and LHP perovskites. Nevertheless, it is well-known that the low stability of these materials at ambient conditions hinders its commercialization and upscaling to the industrial level. For instance, the Cs₃Bi₂X₉ (X = Cl, Br) family showed apparent stability after 5 h of simulated solar light [104]; meanwhile, the A₃Bi₂I₉ (A = Rb, Cs, and MA) structure remained constant after 7 days of exposure to humidity (70%) and UV irradiation (305 nm) [98]. However, there is no evidence regarding the recycling of these materials in consecutive cycles of evaluation. Considering this, several authors have proposed different strategies to increase the stability of the halide perovskites. These are discussed in the next section.

5.3. Stability Strategies for Bismuth Halide Perovskites

Bismuth halide perovskites have emerged as promising candidates for CO₂RR. The efficiency of these materials for CO and CH₄ production from CO₂RR has increased through the optimization of their perovskite structure and the engineering of suitable synthesis methods. Despite these advancements, the instability of the A₃Bi₂X₉ family to environmental factors (e.g., humidity, light, oxygen, or temperature) is one of the most critical factors limiting their application and, thus, their commercialization. Under different envi-

ronmental conditions, these materials can undergo morphological and structural changes and lower light absorption, negatively affecting their photocatalytic performance [106–109]. For example, in the presence of water, the halide perovskites tend to hydrolyze back to their precursors. Specifically, water can penetrate the perovskite lattice to form mono- and di-hydrated perovskite phases in which the A (Cs^+ and Bi^{3+}) cations are no longer strongly bonded to the octahedral; as a result, a phase segregation of Al_2 crystals takes place (Equation (4)). Then, the hydrolysis of Al_2 occurs to promote the formation of bismuth oxyhalides (BiOX , $X = \text{I}, \text{Br}, \text{Cl}$) (Equation (5)) [108]. Furthermore, water can protonate the excess halide to form an acid (HX), which is highly volatile at room temperature. Therefore, the continuous release of these compounds can drive the decomposition of the perovskite layer, decreasing the efficiency of photocatalytic reactions, such as CO_2RR .



On the other hand, the combination of oxygen and light can also promote the decomposition of the bismuth halide perovskites through a photo-oxidation process [109]. This process occurs due to the photocatalytic properties of the material itself and starts with the absorption of light with energy equal to or higher than the band gap value of the material, which promotes an electron transfer from the CB to the VB. Then, the photogenerated electrons in the perovskite react with the adsorbed O_2 to form superoxide radicals ($\text{O}_2^{\cdot-}$), which can start the decomposition of this material. This process has been previously demonstrated in the MAPbI_3 perovskite [109,110], and its mechanism is schematized in Figure 5. The first step is the oxygen diffusion into the lattice (Figure 5a), then the light absorption in the perovskite leads to the generation of electrons and holes (Figure 5b), which react with the adsorbed oxygen to generate the superoxide radicals (Figure 5c). Finally, this, promotes the degradation of the perovskite to PbI_2 , H_2O , I_2 , and CH_3NH_2 (Figure 5d) [109].

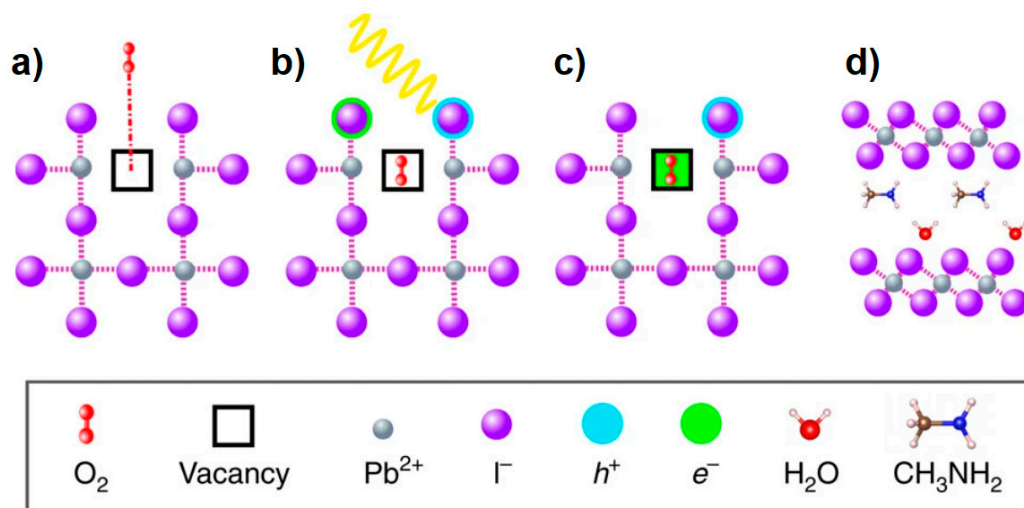


Figure 5. Schematic mechanism of the degradation of the perovskite structure (e.g., $\text{CH}_3\text{NH}_3\text{PbI}_3$) by the action of oxygen under light conditions: (a) oxygen diffusion, (b) Light absorption, (c) Formation of superoxide radicals, and (d) degradation of the perovskite. Adapted from [109].

Considering these scenarios and the degradation mechanisms, several strategies have been proposed to increase halide perovskites' stability, which are summarized in Figure 6. These strategies can be classified into two different approaches:

- (a) **Intrinsic.** This approach is widely used to improve the stability of metal halide perovskites through structural modification, which involves the alteration of the composition of cations and anions that are inherent to the perovskite structure [111,112]. The formation of solid solutions and double perovskites are examples of this approach.

Likewise, the obtention of low-dimensional-networked perovskites promotes the formation of more stable crystal structures by selecting appropriate manufacturing techniques. Stoichiometry modification then settles the network in a quasi-zero-dimensional (0D) configuration, where the metal halide octahedra are almost isolated [113]. Another successfully intrinsic strategy is passivation [114]. This strategy allows the removal of dangling bonds, which act as recombination centers associated with defects, promoting better stability and optical properties. Antisolvent engineering is another strategy that speeds up nucleation during perovskite synthesis through solvent extraction [115–117]. This strategy allows the obtention of dense, high-quality films of bismuth halide perovskites with enhanced stability.

- (b) Extrinsic. This approach is characterized by the modification of the perovskite's external properties without altering its internal composition. Among these strategies, encapsulation is one of the most used. It consists of the coverage of the perovskite to prevent exposure to moisture, oxygen, UV light, and temperature, thus protecting the structure. The encapsulation can be done by glass–glass covering of the edges of the substrate with an adhesive, as well as the deposition of a polymer coating. The adhesives can be ethylene methacrylate (EMA), ethylene vinyl acetate (EVA), polyisobutylene (PIB), and epoxy resins activated with UV light [118]. Alternatively, encapsulation can be done by depositing polymer coatings, e.g., polyethylene oxide, polyvinyl pyridine. The construction of heterostructures or Z-schemes between perovskites and other semiconductors has contributed to the design of promising stabilities for photocatalytic reactions, since electrons are not available to react with the adsorbed oxygen. This avoids the degradation of the perovskite structure [119–121]. Another option is the dispersion of the perovskite nanoparticles in porous support for enhanced electron and hole separation, more accessible active sites, and close contact with the reaction species [54]. At the same time, adding adequate reactants to the medium can promote good stability of the perovskite structure. For example, it has been proved that the addition of HI during the evaluation of $\text{MA}_3\text{Bi}_2\text{I}_9$ promotes an excellent phase stability and enhanced photocatalytic activity for H_2 evolution [122].

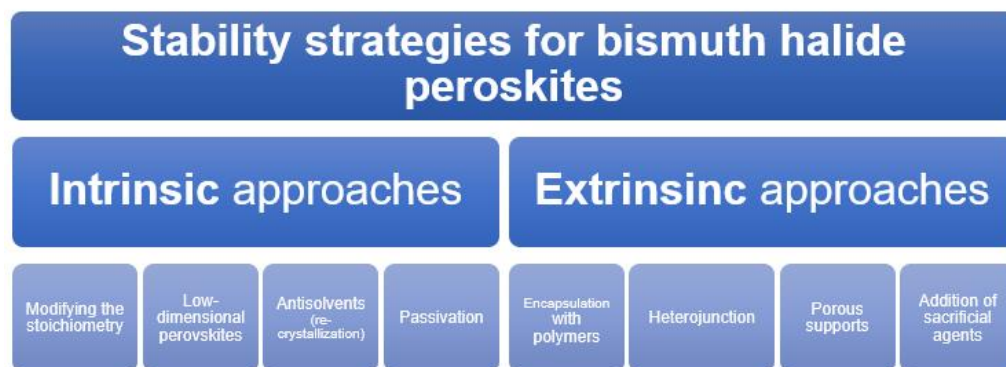


Figure 6. Current strategies proposed to increase the stability of bismuth halide perovskites.

Some of these strategies have been implemented in bismuth halide perovskites to achieve better stabilities and efficiencies in photocatalytic CO_2RR , mainly for $\text{Cs}_3\text{Bi}_2\text{X}_9$ perovskites. The implementation of these strategies for other isostructural materials has not been reported so far. Thus, these applied approaches in $\text{Cs}_3\text{Bi}_2\text{X}_9$ will be discussed in the following section.

5.4. Implemented Strategies to Increase the Efficiency and Stability of the $\text{Cs}_3\text{Bi}_2\text{X}_9$ Family in CO_2RR

As previously mentioned, the most widely studied materials in the $\text{A}_3\text{Bi}_2\text{X}_9$ family for photocatalytic CO_2RR uses Cs^+ as the A-site cation. So far, the stability of the $\text{Cs}_3\text{Bi}_2\text{X}_9$ perovskite has been boosted by implementing two intrinsic (solid solutions and double perovskites) and two extrinsic (the formation of heterojunctions with other semiconductors and the encapsulation of the perovskites in porous supports) approaches.

5.4.1. Intrinsic Approaches to Improve the Stability of $\text{Cs}_3\text{Bi}_2\text{X}_9$ in CO₂RR

(a) Solid solutions

The formation of solid solutions enables more stable structures than their unmixed counterparts because increasing the availability of configuration states also increases the configurational entropy of the system [123]. A recent report proposed the synthesis of $\text{Cs}_3\text{Bi}_2\text{X}_9$ ($X = \text{Cl}, \text{Cl}_{0.5}\text{Br}_{0.5}, \text{Br}, \text{Br}_{0.5}\text{I}_{0.5}, \text{I}$) by solution recrystallization and demonstrated that this set of materials exhibited suitable band gaps and energy band positions to achieve CO production from CO₂RR [124]. The $\text{Cs}_3\text{Bi}_2(\text{Br}_{0.5}\text{I}_{0.5})_9$ solution showed an optimal photoreduction performance for CO generation ($54 \mu\text{mol g}^{-1}$ in 3 h) with 100% selectivity upon visible light irradiation. This efficiency is almost five times higher compared to $\text{Cs}_3\text{Bi}_2\text{I}_9$, which is attributed to a suitable band gap structure, wide light absorption range, and higher photocurrent. Furthermore, there was no obvious decrease in the CO evolution rate during 10 h of irradiation, which indicated that the solid solution might have moderate stability under these conditions.

(b) Double perovskites

Research on double perovskites has recently grown in importance due to their higher stability and nontoxicity compared to the widely used lead halide perovskites. Replacing two divalent (Pb^{2+}) ions with heterovalent cations (e.g., one trivalent and one monovalent cation) leads to the formation of double perovskites.

In double perovskites (of $\text{A}_2\text{BB}'\text{X}_6$ formula), two toxic divalent lead ions are replaced by nontoxic monovalent (B) and trivalent metal ions (B'), which neutralize the overall charge in the conventional perovskites. Double perovskites owe their name to the fact that their unit cell is twice the cell of metal halide perovskites [125].

In the search for alternative photocatalytic materials with improved stability for CO₂RR, some double perovskite materials have been proposed based on the incorporation of Ag as a monovalent cation and Bi as a trivalent cation [126–131]. The efficiency of the double perovskite $\text{Cs}_2\text{AgBiX}_6$ ($X = \text{I}, \text{Cl}, \text{Br}$) has been demonstrated in the generation of CO from CO₂RR [126,129]. These works also evidenced that the $\text{Cs}_2\text{AgBiBr}_6$ nanoplates showed a more than 8-fold enhancement compared to nanocubes of the same perovskite ($255 \mu\text{mol g}^{-1}$ vs. $31 \mu\text{mol g}^{-1}$). This improvement of photocatalytic performance was related to the anisotropically confined charge carriers and their in-plane long diffusion length for the nanoplates compared to nanocubes.

The stability of $\text{Cs}_2\text{AgBiBr}_6$ was recently demonstrated by Zhou et al. [128]. They investigated the stability of this double perovskite under different solvents after 21 days of exposure. The different solvents employed were polar (dimethyl formamide, acetone), protonic (isobutanol), mild polar (ethyl acetate, chloroform), and nonpolar (octane). The results are shown in Figure 7. The perovskite was decomposed by most of the solvents studied due to their strong polarity and the dynamic equilibrium between bound and free ligands, leading to the degradation of $\text{Cs}_2\text{AgBiBr}_6$. In contrast, the perovskite showed superior stability in chloroform and octane for more than 3 weeks. Furthermore, the use of ethyl acetate allowed for the stabilization of the perovskite for 5 days. Therefore, these results offered an opportunity for upcoming research on the CO₂RR by using double halide perovskites. Under this approach, the production of CO and CH₄ was 14 and 9 $\mu\text{mol g}^{-1}$, respectively [128,130].

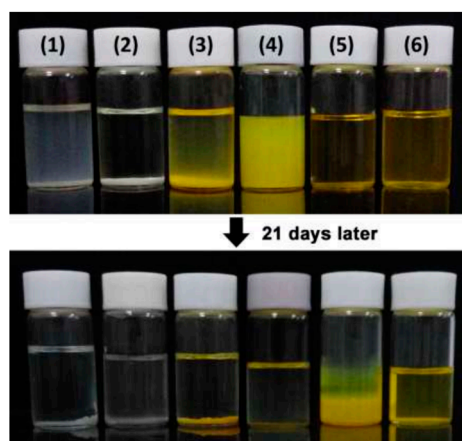


Figure 7. Photos of the double perovskite $\text{Cs}_2\text{AgBiBr}_6$ dispersed in various the solvents: (1) dimethyl formamide, (2) acetone, (3) isobutanol, (4) ethyl acetate, (5) chloroform, and (6) octane [128].

5.4.2. Extrinsic Approaches to Improve the Stability of $\text{Cs}_3\text{Bi}_2\text{X}_9$ in CO₂RR

(a) Heterojunctions of $\text{Cs}_3\text{Bi}_2\text{X}_9$ with other semiconductors

The use of heterostructured materials has resulted in outstanding efficiencies in different photocatalytic reactions [132]. Remarkably, their use in photocatalytic CO₂RR has allowed for the control of selectivity [133], the enhancement of the charge transfer, and, thus, an increase in the production of different solar fuels [134–136]. Considering this, various research groups have recently proposed implementing this extrinsic approach to increase the stability of bismuth halide perovskite.

Liu et al. proposed an interesting heterojunction based on $\text{Cs}_3\text{Bi}_2\text{I}_9/\text{Bi}_2\text{WO}_6$ [137]. They suggested that cosharing the Bi atom enabled intimate contact and strong electron coupling between both perovskites, which eventually increased the interfacial charge transfer through the Z-scheme pathway. The band potentials of each semiconductor were obtained from Mott–Schottky plots, which served as the basis for the proposal of the band coupling of $\text{Cs}_3\text{Bi}_2\text{I}_9/\text{Bi}_2\text{WO}_6$. The Fermi energy level of the halide perovskite was higher than that of Bi_2WO_6 , which suggested that the electrons in Bi_2WO_6 tend to migrate to $\text{Cs}_3\text{Bi}_2\text{I}_9$ to balance the Fermi energy level, promoting an electron cloud coupling between both materials, as shown in Figure 8a. Additionally, the authors proposed that Bi_2WO_6 favors H_2O oxidation; meanwhile, $\text{Cs}_3\text{Bi}_2\text{I}_9$ favors CO_2 reduction. This phenomenon accords with the low CO production observed in the Bi_2WO_6 reference, whereas the heterojunction promoted the highest CO generation ($66 \mu\text{mol g}^{-1}$), which is over four times higher than its reference $\text{Cs}_3\text{Bi}_2\text{I}_9$ (Figure 8b). On the other hand, the stability of the heterojunction was confirmed after three cycling tests. The results indicated that the $\text{Cs}_3\text{Bi}_2\text{I}_9\text{-Bi}_2\text{WO}_6$ heterojunction retains its activity after different evaluations (Figure 8c). The X-ray diffraction results evidenced that the crystalline phases of both materials remained, demonstrating its good stability in the gas–solid reaction system under simulated sunlight irradiation.

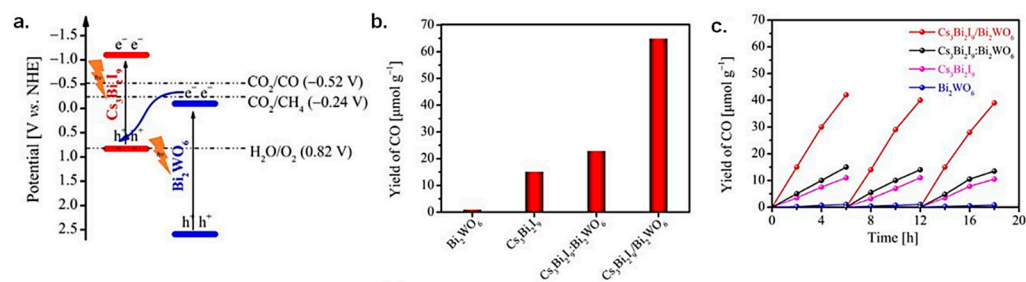


Figure 8. Implementation of an extrinsic approach to increase the efficiency and stability of Cs₃Bi₂I₉: (a) Band coupling, (b) Comparative CO generation, and (c) Stability tests of Cs₃Bi₂I₉–Bi₂WO₆ heterojunction. Adapted from [137].

Cerium oxide (CeO₂) is another semiconductor that was proposed to form a heterostructure with Cs₃Bi₂I₉. This oxide is known to possess a good CO₂ affinity [138], which is a prerequisite to designing alternative photocatalyst materials to assure high efficiencies in CO₂RR. Therefore, Feng et al. synthesized the Cs₃Bi₂I₉–CeO₂ Z-scheme heterojunction by a self-template-oriented method using BiOI–Bi₂O_{2.7} nanosheets as a template and Bi precursor [139]. The authors also proposed a charge transfer mechanism similar to the one previously discussed by Liu et al. In this mechanism, the electrons in CeO₂ are transferred to the perovskite to reduce the CO₂ molecule to CO and CH₄. As a result, the total yield of the products (CO/CH₄) reached 238 μmol g⁻¹, and the electron consumption yield was calculated as 877 μmol g⁻¹, which is 7 and 15 times higher than the reference materials, respectively. It is important to highlight that this is the best efficiency obtained so far among the reported bismuth-based perovskite (Table 1). Also, the authors investigated the stability of Cs₃Bi₂I₉–CeO₂ after five consecutive cycles and found that in the first three cycles (12 h), the activity remains; however, the activity partially decreased after the fourth (71%) and fifth cycles (55%), suggesting that the catalyst showed good stability in the first 12 h of reaction.

Another option to design heterojunctions with bismuth halide perovskites is by using sulfurs. Zhang et al. proposed an S-scheme based on the coupling of Cs₃Bi₂Br₉ with In₄SnS₈ [140]. The authors demonstrated that the coupling of both semiconductors boosted the charge separation by forming an internal electric field by in situ irradiated X-ray photoelectron spectroscopy, electron spin resonance, femtosecond time-resolved absorption spectroscopy, and density functional theory calculations. The Cs₃Bi₂Br₉–In₄SnS₈ heterojunction exhibits activity towards CO generation (9.5 μmol g⁻¹ h⁻¹) from CO₂RR with high selectivity (92.9%), with results up to 3.8 times higher than the pristine materials. The high selectivity was associated with a decreased energy barrier in the CO₂ reduction to CO through an adsorbed *COOH intermediate.

In addition, the combination of two approaches has been proposed to increase the stability of the bismuth halide perovskites. Zhang et al. synthesized the double perovskite Cs₂AgBiBr₆ on the surface of MXene nanosheets [131]. Here, MXene (M_{n+1}X_nT_x) reduces the exciton binding energy of the double perovskite and simultaneously promotes a more efficient formation of the charge carriers. The combination of these strategies promoted the formation of CO (11.1 μmol g⁻¹), CH₄ (1.3 μmol g⁻¹), and H₂ (8.9 μmol g⁻¹) under visible irradiation. The apparent quantum yield showed values of 0.083%, 0.071%, and 0.005% at 485, 535, and 595 nm, respectively.

(b) Encapsulation in porous supports

The encapsulation of bismuth halide perovskites is another option to provide stability through their support on porous materials. Previous studies suggest that mesoporous encapsulation enhances the stability of halide perovskites and prevents halide ion exchange [141]. However, it is still unclear whether the mesoporous structure provides stability against moisture, since H₂O molecules can penetrate into the pores to degrade the perovskite. Even so, a recent report demonstrated good stability in the Cs₃Bi₂Br₉ perovskite encapsulated in the porous structure of the MCM-41 molecular sieve, as is shown

in Figure 9a. This strategy allows the stable production of CO ($17 \mu\text{mol g}^{-1} \text{h}^{-1}$) after 8 consecutive cycles (Figure 9b) [142].

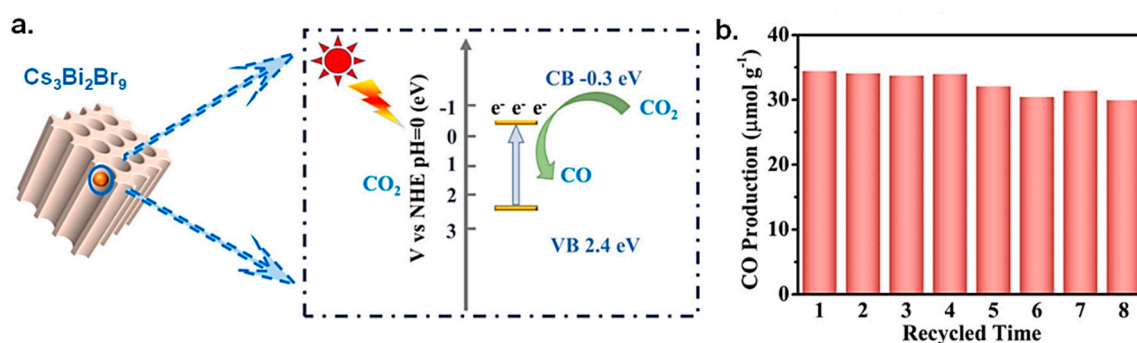


Figure 9. (a) Schematic representation of the encapsulation of $\text{Cs}_3\text{Bi}_2\text{Br}_9$ on MCM-41 and (b) cycling experiment tests. Adapted from [142].

Similarly, the implementation of extrinsic and intrinsic strategies allowed for the obtention of the double perovskite $\text{Cs}_2\text{AgBiBr}_6$ grown on mesoporous TiO_2 nanoparticles that provide remarkably high stability for CH_4/CO generation, which was recently proposed by Sun et al. [127]. This work reports the best selectivity (88.7%) for CH_4 generation compared to other lead and bismuth halide perovskites. This result was associated with the high CO_2 uptake of the mesoporous support ($3.4 \text{ cm}^3 \text{ g}^{-1}$) and the Bi-active sites, which mediate the hydrogenation of CO ($^*\text{HCO}$) under light irradiation. Also, the presence of TiO_2 suggests a possible heterostructure formation with $\text{Cs}_2\text{AgBiBr}_6$, enhancing the charge transfer.

Table 1. Summary of the solar fuels obtained from CO2RR by the implementation of different stability strategies in the $\text{Cs}_3\text{Bi}_2\text{X}_9$ perovskites.

Material	Morphology	Product ($\mu\text{mol g}^{-1}$)	Irradiation	Reaction Medium	Stability	Ref.
$\text{Cs}_3\text{Bi}_2\text{X}_9$ ($X = \text{Cl}, \text{Br}, \text{I}$)	Quantum dots	CO (135)	AM 1.5G	$\text{H}_2\text{O}_{\text{vapor}}$	5 h	[104]
$\text{A}_3\text{Bi}_2\text{I}_9$ ($A = \text{Rb}^+, \text{Cs}^+$ or $\text{CH}_3\text{NH}_3^+, \text{MA}^+$)	Nanoparticles	CO (77) CH_4 (5)	UV lamp (32 W, 305 nm)	Trichloromethane	12 h	[98]
$\text{Cs}_3\text{Bi}_2\text{X}_9$ ($X = \text{Cl}, \text{Cl}_{0.5}\text{Br}_{0.5},$ $\text{Br}, \text{Br}_{0.5}\text{I}_{0.5}, \text{I}$)	Nanocrystals	CO (54)	Xenon lamp (300 W, 420 nm)	$\text{H}_2\text{O}_{\text{vapor}}$	10 h	[124]
$\text{Cs}_2\text{AgBiX}_6$ ($X = \text{Cl}, \text{Br}, \text{I}$)	Nanoplatelets	CO (40) CH_4 (25)	Laser (405 nm)	Ethyl acetate	6 h	[126]
$\text{Cs}_2\text{AgBiBr}_6$	Cubic	CO (14) CH_4 (9)	AM 1.5G (100 W)	Ethyl acetate	21 days	[128]
$\text{Cs}_2\text{AgBiI}_6$	Quasi-spherical	CO (19)	Xenon lamp (300 W, 420 nm)	Toluene	3 h	[129]
$\text{Cs}_2\text{AgBiBr}_6$ / TiO_2	Spheres	CO (20) CH_4 (151)	Xenon lamp (300 W, 70 mW/cm^2)	Isopropyl alcohol	5 h (5 cycles)	[127]
$\text{Cs}_2\text{AgBiBr}_6$ / $g\text{-C}_3\text{N}_4$	Semi-spheres	CO (1.8) CH_4 (0.2)	AM 1.5G	Ethyl acetate and methanol	12 h (4 cycles)	[130]
$\text{Cs}_2\text{AgBiBr}_6$ / MXene	Nanocrystals	CO (11) CH_4 (1) H_2 (9)	Xenon lamp (400 nm)	$\text{H}_2\text{O}_{\text{vapor}}$	5 h (3 cycles)	[131]
$\text{Cs}_3\text{Bi}_2\text{I}_9$ / Bi_2WO_6	Nanosheets	CO (65)	Xenon lamp (300 W, 100 mW/cm^2)	$\text{H}_2\text{O}_{\text{vapor}}$	5 h (3 cycles)	[137]
$\text{Cs}_3\text{Bi}_2\text{I}_9$ / CeO_2	Nanosheets	CO (170) CH_4 (65)	Xenon lamp (300 W)	$\text{H}_2\text{O}_{\text{vapor}}$	12 h (5 cycles)	[139]

Table 1. Cont.

Material	Morphology	Product ($\mu\text{mol g}^{-1}$)	Irradiation	Reaction Medium	Stability	Ref.
$\text{Cs}_3\text{Bi}_2\text{Br}_9$ / In_4SnS_8	Quantum dots	CO (60)	Xenon lamp (300 W)	$\text{H}_2\text{O}_{\text{vapor}}$ (80 kPa)	8 h (3 cycles)	[140]
$\text{Cs}_3\text{Bi}_2\text{Br}_9$ / MCM-41	Nanoparticles	CO (34)	Xenon lamp (300 W, 420 nm)	$\text{H}_2\text{O}_{\text{vapor}}$	2 h (8 cycles)	[142]

5.5. General Remarks

Table 1 lists the reports of bismuth halide perovskites for CO₂RR and the stability reached within each system. As is shown, the stability of the bismuth halide perovskites in gas–solid reactions varies from 5 h to 21 days. In general, to assure good efficiencies, the literature suggests the addition of organic solvents (e.g., ethyl acetate, trichloromethane, toluene, or isopropyl alcohol). However, this strategy makes it difficult to differentiate the actual capacity of the perovskites to produce solar fuels from CO₂RR. Also, the use of double perovskites shows promising results to obtain materials with remarkably high selectivity for products such as CH₄, which can be directly used for the generation of clean and sustainable energy.

So far, the best result for CO generation was obtained with the $\text{Cs}_3\text{Bi}_2\text{I}_9$ – CeO_2 heterostructure ($135 \mu\text{mol g}^{-1}$), whereas the implementation of three stability strategies such as double perovskites, encapsulation, and heterostructures allowed for the highest efficiency in producing CH₄ ($151 \mu\text{mol g}^{-1}$). Both efficiencies (with good stability during the evaluation) demonstrated the feasibility of using CO₂RR to generate clean and renewable solar fuels.

6. Next Steps to Design and Evaluate Bismuth Halide Perovskites in CO₂RR

Thus far, there is a limited number of reports of using bismuth halide perovskites for CO₂RR despite their interesting and remarkable properties, ideal for this reaction. This opens a window of opportunity to implement stability strategies to achieve better efficiencies in this process for the larger scale.

According to the literature reviewed, some phenomena remain to be further investigated in this field. First, it seems that the halide anion (X) and A cation selection in the $\text{A}_3\text{Bi}_2\text{X}_9$ structure influences the photocatalytic performance of the perovskite in CO₂RR. Particularly, there have been better results for CO₂RR with the use of Br as X and Cs as A cation for CO generation, as well as Rh as A cation for CH₄ production. Nevertheless, other cations of smaller size, such as K, have not been explored in the study of the $\text{A}_3\text{Bi}_2\text{X}_9$ family.

What is more, there are no reports about the possible formation of a heterostructure employing bismuth oxyhalides (BiOX) and bismuth halide perovskites, mostly because of their interaction with H₂O (equations (4) and (5)). This would be interesting, since the cosharing Bi and X atoms could promote better interaction with the components. This type of passivation on perovskites opens the possibility of their evaluation in batch reactors in the liquid medium to produce liquids products (e.g., HCOOH, HCOH, CH₃OH, CH₃CH₂OH), which offers great advantages related to their intrinsic chemical energy content and the eases of implementation, along with storage and transportation. Furthermore, the encapsulation of bismuth halide perovskites in polymeric films has not been explored.

In addition, it was demonstrated that combining extrinsic and intrinsic approaches is critical to assure good efficiencies and remarkable stabilities for bismuth halide perovskites in CO₂RR. Therefore, when scientists begin designing bismuth halide perovskites, it is vital to implement at least one stability strategy to ensure good efficiencies and allow the community to move forward with scaling the CO₂RR process.

Another critical factor is the need for a standardization process for reactor design, operational parameters (e.g., temperature, pressure, or flow mass), light source and filters, as well as solvents to assure a fair comparison of the efficiencies obtained, which will

eventually promote the scaling of CO₂RR at the industrial level to the continuous operation of solar refineries that use the CO₂ emissions, H₂O, and solar light as raw materials. All these critical steps to design new and more efficient bismuth halide perovskites are summarized in Figure 10.

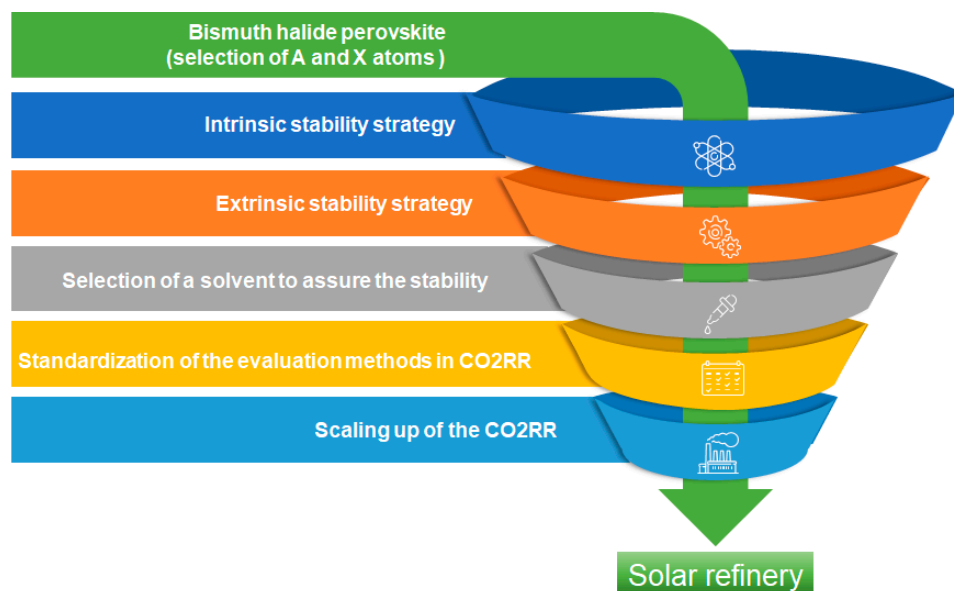


Figure 10. Next steps to design bismuth halide perovskites.

7. Conclusions and Perspectives

This review aims to summarize the stability strategies recently proposed for bismuth halide perovskite to assure high efficiencies in CO₂RR. This topic is highly interesting for the scientific community since bismuth halide perovskites have enormous potential to be used in CO₂RR to generate clean and renewable solar fuels. However, although significant progress has been achieved in bismuth halide perovskites, there are still many challenges regarding their stability, selectivity, and efficiency for continuous solar fuel generation.

The stability strategies of the bismuth halide perovskites have been classified into two approaches: intrinsic and extrinsic. The first approach is related to the modification of the bismuth halide's crystal structure by forming solid solutions or by adding a second cation to improve the stability of the materials against O₂, H₂O, and light. On the other hand, the second approach is associated with incorporating additional components to the perovskite to maintain its stability (e.g., heterojunctions, encapsulation on porous supports, and modifying the reaction parameters). The reports so far evidence that it is necessary to include at least one stability strategy of each approach to obtain highly stable structures with remarkable efficiencies and selectivity to produce solar fuels.

This study tries to provide a brief guide for scientists in designing new and advanced bismuth halide perovskites with high stability using different strategies that boost their practical applications in artificial photosynthesis.

Author Contributions: Conceptualization, E.L.-H. and L.M.T.-M.; methodology, O.L.Q.-L.; validation, E.L.-H. and L.M.T.-M.; formal analysis, E.L.-H. and O.L.Q.-L.; investigation, E.L.-H. and O.L.Q.-L.; resources, L.M.T.-M. and E.L.-H.; data curation, O.L.Q.-L. and E.L.-H.; writing—original draft preparation, E.L.-H. and O.L.Q.-L.; supervision, Leticia M. Torrez-Martínez; project administration, E.L.-H.; funding acquisition, E.L.-H.. All authors have read and agreed to the published version of the manuscript.

Funding: The authors thank Consejo Nacional de Ciencia y Tecnología for financial support through the projects: Paradigmas y Fronteras de la Ciencia 320379 and Cátedras CONACYT 1060.

Conflicts of Interest: The authors declare no conflict of interest.

References

1. IEA. Global Energy Review: CO₂ Emissions in 2021—Analysis. 2021. Available online: <https://www.iea.org/reports/global-energy-review-co2-emissions-in-2021-2> (accessed on 1 September 2022).
2. Energy Agency, I. Global Energy Review: CO₂ Emissions in 2021 Global Emissions Rebound Sharply to Highest Ever Level. 2021. Available online: www.iea.org/t&c/ (accessed on 1 September 2022).
3. Ponce, P.; Khan, S.A.R. A causal link between renewable energy, energy efficiency, property rights, and CO₂ emissions in developed countries: A road map for environmental sustainability. *Environ. Sci. Pollut. Res.* **2021**, *28*, 37804–37817. [[CrossRef](#)] [[PubMed](#)]
4. Answer, M.K.; Iqbal, W.; Ahmad, U.S.; Fatima, A.; Chaudhry, I.S. Environmental efficiency and the role of energy innovation in emissions reduction. *Environ. Sci. Pollut. Res.* **2020**, *27*, 29451–29463. [[CrossRef](#)] [[PubMed](#)]
5. Salehizadeh, H.; Yan, N.; Farnood, R. Recent advances in microbial CO₂ fixation and conversion to value-added products. *Chem. Eng. J.* **2020**, *390*, 124584. [[CrossRef](#)]
6. Meunier, N.; Chauvy, R.; Mouhoubi, S.; Thomas, D.; De Weireld, G. Alternative production of methanol from industrial CO₂. *Renew. Energy* **2020**, *146*, 1192–1203. [[CrossRef](#)]
7. Kumaravel, V.; Bartlett, J.; Pillai, S.C. Photoelectrochemical Conversion of Carbon Dioxide (CO₂) into Fuels and Value-Added Products. *ACS Energy Lett.* **2020**, *5*, 486–519. [[CrossRef](#)]
8. Garba, M.D.; Usman, M.; Khan, S.; Shehzad, F.; Galadima, A.; Ehsan, M.F.; Ghanem, A.S.; Humayun, M. CO₂ towards fuels: A review of catalytic conversion of carbon dioxide to hydrocarbons. *J. Environ. Chem. Eng.* **2021**, *9*, 104756. [[CrossRef](#)]
9. Mustafa, A.; Lougou, B.G.; Shuai, Y.; Wang, Z.; Tan, H. Current technology development for CO₂ utilization into solar fuels and chemicals: A review. *J. Energy Chem.* **2020**, *9*, 96–123. [[CrossRef](#)]
10. Gong, E.; Ali, S.; Hiragond, C.B.; Kim, H.S.; Powar, N.S.; Kim, D.; Kim, H.; In, S.-I. Solar fuels: Research and development strategies to accelerate photocatalytic CO₂ conversion into hydrocarbon fuels. *Energy Environ. Sci.* **2022**, *15*, 880–893. [[CrossRef](#)]
11. Patial, S.; Kumar, R.; Raizada, P.; Singh, P.; Le, Q.V.; Lichtfouse, E.; Nguyen, D.L.T.; Nguyen, V.-H. Boosting light-driven CO₂ reduction into solar fuels: Mainstream avenues for engineering ZnO-based photocatalysts. *Environ. Res.* **2021**, *197*, 111134. [[CrossRef](#)]
12. Omr, H.A.E.; Horn, M.W.; Lee, H. Low-Dimensional Nanostructured Photocatalysts for Efficient CO₂ Conversion into Solar Fuels. *Catalysts* **2021**, *11*, 418. [[CrossRef](#)]
13. Shen, Y.; Han, Q.; Hu, J.; Gao, W.; Wang, L.; Yang, L.; Gao, C.; Shen, Q.; Wu, C.; Wang, X.; et al. Artificial Trees for Artificial Photosynthesis: Construction of Dendrite-Structured α -Fe₂O₃/g-C₃N₄ Z-Scheme System for Efficient CO₂ Reduction into Solar Fuels. *ACS Appl. Energy Mater.* **2020**, *3*, 6561–6572. [[CrossRef](#)]
14. Burke, R.; Bren, K.L.; Krauss, T.D. Semiconductor nanocrystal photocatalysis for the production of solar fuels. *J. Chem. Phys.* **2021**, *154*, 030901. [[CrossRef](#)] [[PubMed](#)]
15. Xia, Y.; Zhang, L.; Hu, B.; Yu, J.; Al-Ghamdi, A.A.; Wageh, S. Design of highly-active photocatalytic materials for solar fuel production. *Chem. Eng. J.* **2021**, *421*, 127732. [[CrossRef](#)]
16. Yu, S.; Wilson, A.J.; Heo, J.; Jain, P.K. Plasmonic Control of Multi-Electron Transfer and C–C Coupling in Visible-Light-Driven CO₂ Reduction on Au Nanoparticles. *Nano Lett.* **2018**, *18*, 2189–2194. [[CrossRef](#)] [[PubMed](#)]
17. Fu, J.; Jiang, K.; Qiu, X.; Yu, J.; Liu, M. Product selectivity of photocatalytic CO₂ reduction reactions. *Mater. Today* **2020**, *32*, 222–243. [[CrossRef](#)]
18. Liu, Z.; Wang, Z.; Qing, S.; Xue, N.; Jia, S.; Zhang, L.; Li, L.; Li, N.; Shi, L.; Chen, J. Improving methane selectivity of photo-induced CO₂ reduction on carbon dots through modification of nitrogen-containing groups and graphitization. *Appl. Catal. B.* **2018**, *232*, 86–92. [[CrossRef](#)]
19. Tu, W.; Li, Y.; Kuai, L.; Zhou, Y.; Xu, Q.; Li, H.; Wang, X.; Xiao, M.; Zou, Z. Construction of unique two-dimensional MoS₂–TiO₂ hybrid nanojunctions: MoS₂ as a promising cost-effective cocatalyst toward improved photocatalytic reduction of CO₂ to methanol. *Nanoscale* **2017**, *9*, 9065. [[CrossRef](#)]
20. Zhang, H.; Wang, T.; Wang, J.; Liu, H.; Dao, T.D.; Li, M.; Liu, G.; Meng, X.; Chang, K.; Shi, L.; et al. Surface-Plasmon-Enhanced Photodriven CO₂ Reduction Catalyzed by Metal–Organic-Framework-Derived Iron Nanoparticles Encapsulated by Ultrathin Carbon Layers. *Adv. Mat.* **2016**, *28*, 3703–3710. [[CrossRef](#)]
21. Low, J.; Yu, J.; Ho, W. Graphene-Based Photocatalysts for CO₂ Reduction to Solar Fuel. *J. Phys. Chem. Lett.* **2015**, *6*, 4244–4251. [[CrossRef](#)]
22. Wang, W.-N.; An, W.-J.; Ramalingam, B.; Mukherjee, S.; Niedzwiedzki, D.M.; Gangopadhyay, S.; Biswas, P. Size and Structure Matter: Enhanced CO₂ Photoreduction Efficiency by Size-Resolved Ultrafine Pt Nanoparticles on TiO₂ Single Crystals. *J. Am. Chem. Soc.* **2012**, *134*, 11276–11281. [[CrossRef](#)]
23. Wang, J.; Li, H.; Gao, P.; Peng, Y.; Cao, S.; Antonietti, M. CsPbBr₃ perovskite based tandem device for CO₂ photoreduction. *Chem. Eng. J.* **2022**, *43*, 136447. [[CrossRef](#)]
24. Liu, P.; Peng, X.; Men, Y.-L.; Pan, Y.-X. Recent progresses on improving CO₂ adsorption and proton production for enhancing efficiency of photocatalytic CO₂ reduction by H₂O. *GreenChE* **2020**, *1*, 33–39. [[CrossRef](#)]
25. Avila-López, M.A.; Tan, J.Z.Y.; Luévano-Hipólito, E.; Torres-Martínez, L.M.; Maroto-Valer, M.M. Production of CH₄ and CO on Cu_xO and Ni_xO_y coatings through CO₂ photoreduction. *J. Environ. Chem. Eng.* **2022**, *10*, 108199. [[CrossRef](#)]

26. Tokudome, Y.; Fukui, M.; Iguchi, S.; Hasegawa, Y.; Teramura, K.; Tanaka, T.; Takemoto, M.; Katsura, R.; Takahashi, M. A nanoLDH catalyst with high CO₂ adsorption capability for photo-catalytic reduction. *J. Mater. Chem.* **2018**, *6*, 9684–9690. [[CrossRef](#)]
27. Fu, J.; Zhu, B.; Jiang, C.; Cheng, B.; You, W.; Yu, J. Hierarchical porous O-doped g-C₃N₄ with enhanced photocatalytic CO₂ reduction activity. *Small* **2017**, *13*, 1603938. [[CrossRef](#)]
28. Michalkiewicz, B.; Majewska, J.; Kądziołka, G.; Bubacz, K.; Mozia, S.; Morawski, A.W. Reduction of CO₂ by adsorption and reaction on surface of TiO₂-nitrogen modified photocatalyst. *J. CO₂ Util.* **2014**, *5*, 47–52. [[CrossRef](#)]
29. Liu, L.; Zhao, H.; Andino, J.M.; Li, Y. Photocatalytic CO₂ reduction with H₂O on TiO₂ nanocrystals: Comparison of anatase, rutile, and brookite polymorphs and exploration of surface chemistry. *ACS Catal.* **2012**, *2*, 1817–1828. [[CrossRef](#)]
30. Xiang, X.; Pan, F.; Li, Y. A review on adsorption-enhanced photoreduction of carbon dioxide by nanocomposite materials. *Adv. Compos. Hybrid Mater.* **2018**, *1*, 6–31. [[CrossRef](#)]
31. Luévano-Hipólito, E.; Torres-Martínez, L.M. Dolomite-supported Cu₂O as heterogeneous photocatalysts for solar fuels production. *Mater. Sci. Semicond. Process.* **2020**, *116*, 105119. [[CrossRef](#)]
32. Ma, Y.; Yi, X.; Wang, S.; Li, T.; Tan, B.; Chen, C.; Majima, T.; Waclawik, E.R.; Zhu, H.; Wang, J. Selective photocatalytic CO₂ reduction in aerobic environment by microporous Pd-porphyrin-based polymers coated hollow TiO₂. *Nat. Commun.* **2022**, *13*, 1400. [[CrossRef](#)]
33. Parvavian, A.M.; Sadeghi, N.; Rafiee, A.; Shearer, C.J.; Jafarian, M. Application of Porous Materials for CO₂ Reutilization: A Review. *Energies* **2022**, *15*, 63. [[CrossRef](#)]
34. Ma, Z.; Wang, Y.; Lu, Y.; Ning, H.; Zhang, J. Tackling Challenges in Perovskite-Type Metal Oxide Photocatalysts. *Energy Technol.* **2021**, *9*, 2001019. [[CrossRef](#)]
35. Inoue, T.; Fujishima, A.; Konishi, S.; Honda, K. Photoelectrocatalytic reduction of carbon dioxide in aqueous suspensions of semiconductor powders. *Nature* **1979**, *277*, 637–638. [[CrossRef](#)]
36. Kamal, K.M.; Narayan, R.; Chandran, N.; Popović, S.; Nazrulla, M.A.; Kovač, J.; Vrtovec, N.; Bele, M.; Hodnik, N.; Likozar, M.M.K.B. Synergistic enhancement of photocatalytic CO₂ reduction by plasmonic Au nanoparticles on TiO₂ decorated N-graphene heterostructure catalyst for high selectivity methane production. *Appl. Catal. B Environ.* **2022**, *307*, 121181. [[CrossRef](#)]
37. Tahir, B.; Tahir, M.; Ghazali, M.; Nawawi, M. Highly stable 3D/2D WO₃/g-C₃N₄ Z-scheme heterojunction for stimulating photocatalytic CO₂ reduction by H₂O/H₂ to CO and CH₄ under visible light. *J. CO₂ Util.* **2020**, *41*, 101270. [[CrossRef](#)]
38. Deng, H.; Xu, F.; Cheng, B.; Yu, J.; Ho, W. Photocatalytic CO₂ reduction of C/ZnO nanofibers enhanced by an Ni-NiS cocatalyst. *Nanoscale* **2020**, *12*, 7206–7213. [[CrossRef](#)] [[PubMed](#)]
39. Wang, S.; Wang, X. Photocatalytic CO₂ reduction by CdS promoted with a zeolitic imidazolate framework. *Appl. Catal. B Environ.* **2015**, *162*, 494–500. [[CrossRef](#)]
40. Xiao, S.; Guan, Y.; Shang, H.; Li, H.; Tian, Z.; Liu, S.; Chen, W.; Yang, J. An S-scheme NH₂-UiO-66/SiC photocatalyst via microwave synthesis with improved CO₂ reduction activity. *J. CO₂ Util.* **2022**, *55*, 101806. [[CrossRef](#)]
41. Galli, F.; Compagnoni, M.; Vitali, D.; Pirola, C.; Bianchi, C.L.; Villa, A.; Prati, L.; Rossetti, I. CO₂ photoreduction at high pressure to both gas and liquid products over titanium dioxide, *Appl. Catal. B Environ.* **2017**, *200*, 386–391. [[CrossRef](#)]
42. Luévano-Hipólito, E.; Torres-Martínez, L.M. Ink-jet printing films of molybdates of alkaline earth metals with scheelite structure applied in the photocatalytic CO₂ reduction. *J. Photochem. Photobiol. A Chem.* **2019**, *368*, 15–22. [[CrossRef](#)]
43. Aguirre-Astrain, A.; Luévano-Hipólito, E.; Torres-Martínez, L.M. Integration of 2D printing technologies for AV₂O₆ (A=Ca, Sr, Ba)-MO (M=Cu, Ni, Zn) photocatalyst manufacturing to solar fuels production using seawater. *Int. J. Hydrog. Energy* **2021**, *46*, 37294–37310. [[CrossRef](#)]
44. Gusain, R.; Kumar, P.; Sharma, O.P.; Jain, S.L.; Khatri, O.P. Reduced graphene oxide–CuO nanocomposites for photocatalytic conversion of CO₂ into methanol under visible light irradiation. *Appl. Catal. B Environ.* **2016**, *181*, 352–362. [[CrossRef](#)]
45. Wang, S.; Cabrero-Antonino, M.; Navalón, S.; Cao, C.-c.; Tissot, A.; Dovgaliuk, I.; Marrot, J.; Martineau-Corcós, C.; Yu, L.; Wang, H.; et al. A Robust Titanium Isophthalate Metal-Organic Framework for Visible-Light Photocatalytic CO₂ Methanation. *Chem* **2020**, *6*, 3409–3427. [[CrossRef](#)]
46. Mateo, D.; Morlanes, N.; Maity, P.; Shterk, G.; Mohammed, O.F.; Gascon, J. Efficient Visible-Light Driven Photochemical Conversion of CO₂ to Methane by Nickel Nanoparticles. *Adv. Funct. Mater.* **2021**, *31*, 2008244. [[CrossRef](#)]
47. Wang, X.; Ng, D.; Du, H.; Hornung, C.H.; Polyzos, A.; Seeber, A.; Li, H.; Huo, Y.; Xie, Z. Copper decorated indium oxide rods for photocatalytic CO₂ conversion under simulated sun light. *J. CO₂ Util.* **2022**, *58*, 101909. [[CrossRef](#)]
48. Luévano-Hipólito, E.; Torres-Martínez, L.M. CO₂ photoreduction with H₂O to C1 and C2 products over perovskite films of alkaline niobates ANbO₃ (A = Li, Na, K). *Fuel* **2022**, *320*, 123934. [[CrossRef](#)]
49. Teramura, K.; Okuoka, S.; Tsuneoka, H.; Shishido, T.; Tanaka, T. Photocatalytic reduction of CO₂ using H₂ as reductant over ATaO₃ photocatalysts (A = Li, Na, K). *Appl. Catal. B.* **2010**, *96*, 565–568. [[CrossRef](#)]
50. Luo, C.; Zhao, J.; Li, Y.; Zhao, W.; Zeng, Y.; Wang, C. Photocatalytic CO₂ reduction over SrTiO₃: Correlation between surface structure and activity. *Appl. Surf. Sci.* **2018**, *447*, 627–635. [[CrossRef](#)]
51. Qin, J.; Lin, L.; Wang, X. A perovskite oxide LaCoO₃ cocatalyst for efficient photocatalytic reduction of CO₂ with visible light. *ChemComm* **2018**, *54*, 2272–2275. [[CrossRef](#)]
52. Raza, M.A.; Li, F.; Que, M.; Zhu, L.; Chen, X. Photocatalytic reduction of CO₂ by halide perovskites: Recent advances and future perspectives. *Mater. Adv.* **2021**, *2*, 7187–7209. [[CrossRef](#)]

53. Sanders, S.; Stümmeler, D.; Pfeiffer, P.; Ackermann, N.; Schimkat, F.; Simkus, G.; Heuken, M.; Baumann, P.K.; Vescan, A.; Kalisch, H. Morphology Control of Organic–Inorganic Bismuth-Based Perovskites for Solar Cell Application. *Phys. Status. Solidi A* **2018**, *215*, 1800409. [[CrossRef](#)]
54. Dai, Y.; Poidevin, C.; Ochoa-Hernández, C.; Auer, A.A.; Tüysüz, H. A Supported Bismuth Halide Perovskite Photocatalyst for Selective Aliphatic and Aromatic C–H Bond Activation. *Angew. Chem.* **2020**, *59*, 5788–5796. [[CrossRef](#)] [[PubMed](#)]
55. Jin, S. Can We Find the Perfect A-Cations for Halide Perovskites? *ACS Energy Lett.* **2021**, *6*, 3386–3389. [[CrossRef](#)]
56. Tao, J.; Liu, X.; Shen, J.; Han, S.; Guan, L.; Fu, G.; Kuang, D.-B.; Yang, S. F-Type Pseudo-Halide Anions for High-Efficiency and Stable Wide-Band-Gap Inverted Perovskite Solar Cells with Fill Factor Exceeding 84%. *ACS Nano* **2022**, *16*, 10798–10810. [[CrossRef](#)]
57. Sun, X.; Ji, L.Y.; Chen, W.W.; Guo, X.; Wang, H.H.; Lei, M.; Wang, Q.; Li, Y.F. Halide anion–fullerene π noncovalent interactions: N-doping and a halide anion migration mechanism in p–i–n perovskite solar cells. *J. Mater. Chem.* **2017**, *5*, 20720–20728. [[CrossRef](#)]
58. Wang, Y.; Zhang, X.; Wang, D.; Li, X.; Meng, J.; You, J.; Yin, Z.; Wu, J. Compositional Engineering of Mixed-Cation Lead Mixed-Halide Perovskites for High-Performance Photodetectors. *ACS Appl. Mater. Interfaces* **2019**, *11*, 28005–28012. [[CrossRef](#)]
59. Yu, Z.; Yang, K.; Yu, C.; Lu, K.; Huang, W.; Xu, L.; Zou, L.; Wang, S.; Chen, Z.; Hu, J.; et al. Steering Unit Cell Dipole and Internal Electric Field by Highly Dispersed Er atoms Embedded into NiO for Efficient CO₂ Photoreduction. *Adv. Funct. Mater.* **2022**, *32*, 2111999. [[CrossRef](#)]
60. Liu, X.; Zhang, Z.; Lin, F.; Cheng, Y. Structural modulation and assembling of metal halide perovskites for solar cells and light-emitting diodes. *InfoMat* **2021**, *3*, 1218–1250. [[CrossRef](#)]
61. Guan, X.; Lei, Z.; Yu, X.; Lin, C.-H.; Huang, J.-K.; Huang, C.-Y.; Feng, L.; Ajayan Vinu, L.; Yi, J.; Wu, T. Low-Dimensional Metal-Halide Perovskites as High-Performance Materials for Memory Applications. *Small* **2022**, *18*, 2203311. [[CrossRef](#)]
62. Ling, X.; Yuan, J.; Ma, W. The Rise of Colloidal Lead Halide Perovskite Quantum Dot Solar Cells. *Acc. Mater. Res.* **2022**, *8*, 866–878. [[CrossRef](#)]
63. Levchuk, I.; Osvet, A.; Tang, X.; Brandl, M.; Perea, J.D.; Hoegl, F.; Matt, G.J.; Hock, R.; Batentschuk, M.; Brabec, C.J. Brightly luminescent and color-tunable formamidinium lead halide perovskite FAPbX (X = Cl, Br, I) colloidal nanocrystals. *Nano Lett.* **2017**, *17*, 2765–2770. [[CrossRef](#)] [[PubMed](#)]
64. Jiang, X.; Ding, Y.; Zheng, S.; Ye, Y.; Li, Z.; Xu, L.; Wang, J.; Li, Z.; Loh, X.J.; Ye, E.; et al. In-Situ Generated CsPbBr₃ Nanocrystals on O-Defective WO₃ for Photocatalytic CO₂ Reduction. *ChemSusChem* **2021**, *15*, e202102295.
65. Chen, Y.; Yin, J.; Wei, Q.; Wang, C.; Wang, X.; Ren, H.; Yu, S.F.; Bakr, O.M.; Mohammed, O.F.; Li, M. Multiple exciton generation in tin–lead halide perovskite nanocrystals for photocurrent quantum efficiency enhancement. *Nat. Photon.* **2022**, *16*, 485–490. [[CrossRef](#)]
66. Gao, W.; Ding, J.; Bai, Z.; Qi, Y.; Wang, Y.; Lv, Z. Multiple excitons dynamics of lead halide perovskite. *Nanophotonics* **2021**, *10*, 3945–3955. [[CrossRef](#)]
67. Lin, C.-C.; Liu, T.-R.; Lin, S.-R.; Boopathi, K.M.; Chiang, C.-H.; Tzeng, W.-Y.; Chien, W.-H.C.; Hsu, H.-S.; Luo, C.-W.; Tsai, H.-Y.; et al. Spin-Polarized Photocatalytic CO₂ Reduction of Mn-Doped Perovskite Nanoplates. *J. Am. Chem. Soc.* **2022**, *144*, 15718–15726. [[CrossRef](#)]
68. Chen, T.; Chen, W.-L.; Foley, B.J.; Lee, S.-H. Origin of long lifetime of band-edge charge carriers in organic–inorganic lead iodide perovskites. *Appl. Phys. Sci.* **2017**, *114*, 7519–7524. [[CrossRef](#)]
69. Manikandan, A.; Slimani, Y.; Dinesh, A.; Khan, A.; Thanrasu, K.; Baykal, A.; Jaganathan, S.K.; Dzudzevic-Cancari, H.; Asirid, A.M. Perovskite’s potential functionality in a composite structure. In *Hybrid Perovskite Composite Materials: Design to Applications*; Woodhead Publishing: Cambridge, UK, 2021; Volume 1, pp. 181–202.
70. Brittan, S.; Adhyaksa, G.W.P.; Garnett, E.C. The expanding world of hybrid perovskites: Materials properties and emerging applications. *MRS Commun.* **2015**, *5*, 7–26. [[CrossRef](#)]
71. Gao, P.; Grätzel, M.; Nazeeruddin, M.K. Organohalide Lead Perovskites for Photovoltaic Applications. *Energy Environ. Sci.* **2014**, *7*, 2448–2463. [[CrossRef](#)]
72. Shahrokhi, S.; Gao, W.; Wang, Y.; Anandan, P.R.; Rahaman, M.Z.; Singh, S.; Wang, D.; Cazorla, C.; Yuan, G.; Liu, J.-M.; et al. Emergence of ferroelectricity in halide perovskites. *Small Methods* **2020**, *4*, 2000149. [[CrossRef](#)]
73. Burger, S.; Grover, S.; Butler, K.T.; Boström, H.L.; Grau-Crespo, R.; Kieslich, G. Tilt and shift polymorphism in molecular perovskites. *Mater Horizon.* **2021**, *8*, 2444–2450. [[CrossRef](#)]
74. Dong, Y.; Zhao, Y.; Zhang, S.; Dai, Y.; Liu, L.; Li, Y.; Chen, Q. Recent advances toward practical use of halide perovskite nanocrystals. *J. Mater. Chem. A* **2018**, *6*, 21729–21746. [[CrossRef](#)]
75. Meyer, E.; Mutukwa, D.; Zingwe, N.; Taziwa, R. Lead-free halide double perovskites: A review of the structural, optical, and stability properties as well as their viability to replace lead halide perovskites. *Metals* **2018**, *8*, 667. [[CrossRef](#)]
76. Han, C.; Zhu, X.; San Martin, J.; Lin, Y.; Spears, S.; Yan, Y. Recent Progress in Engineering Metal Halide Perovskites for Efficient Visible-Light-Driven Photocatalysis. *ChemSusChem* **2020**, *13*, 4005–4025. [[CrossRef](#)] [[PubMed](#)]
77. Wang, J.; Wang, J.; Li, N.; Du, X.; Ma, J.; He, C.; Li, Z. Direct Z scheme 0D/2D heterojunction of CsPbBr₃ quantum dots/Bi₂WO₆ nanosheets for efficient photocatalytic CO₂ reduction. *ACS Appl. Mater. Interfaces* **2020**, *12*, 31477–31485. [[CrossRef](#)]
78. Jin, Z.; Zhang, Z.; Xiu, J.; Song, H.; Gatti, T.; He, Z. A critical review on bismuth and antimony halide based perovskites and their derivatives for photovoltaic applications: Recent advances and challenges. *J. Mater. Chem. A* **2020**, *8*, 16166–16188. [[CrossRef](#)]
79. Liao, J.-F.; Cai, Y.-T.; Li, J.-Y.; Jiang, Y.; Wang, X.-D.; Chen, H.-Y.; Kuang, D.-B. Plasmonic CsPbBr₃–Au nanocomposite for excitation wavelength dependent photocatalytic CO₂ reduction. *J. Energy Chem.* **2021**, *53*, 309–315. [[CrossRef](#)]

80. Fan, Q.; Biesold-McGee, G.V.; Ma, J.; Xu, Q.; Pan, S.; Peng, J.; Lin, Z. Lead-free halide perovskite nanocrystals: Crystal structures, synthesis, stabilities, and optical properties. *Angew Chem. Int. Ed.* **2020**, *59*, 1030–1046. [[CrossRef](#)]
81. Chen, Z.; Hu, Y.; Wang, J.; Shen, Q.; Zhang, Y.; Ding, C.; Bai, Y.; Jiang, G.; Li, Z.; Gaponik, N. Boosting photocatalytic CO₂ reduction on CsPbBr₃ perovskite nanocrystals by immobilizing metal complexes. *Chem. Mater.* **2020**, *32*, 1517–1525. [[CrossRef](#)]
82. Ou, M.; Tu, W.; Yin, S.; Xing, W.; Wu, S.; Wang, H.; Wan, S.; Zhong, Q.; Xu, R. Amino-assisted anchoring of CsPbBr₃ perovskite quantum dots on porous g-C₃N₄ for enhanced photocatalytic CO₂ reduction. *Angew. Chem.* **2018**, *57*, 13570–13574. [[CrossRef](#)]
83. Pan, A.; Ma, X.; Huang, S.; Wu, Y.; Jia, M.; Shi, Y.; Liu, Y.; Wangyang, P.; He, L.; Liu, Y. CsPbBr₃ perovskite nanocrystal grown on MXene nanosheets for enhanced photoelectric detection and photocatalytic CO₂ reduction. *J. Phys. Chem. Lett.* **2019**, *10*, 6590–6597. [[CrossRef](#)]
84. Wang, X.; He, J.; Li, J.; Lu, G.; Dong, F.; Majima, T.; Zhu, M. Immobilizing perovskite CsPbBr₃ nanocrystals on Black phosphorus nanosheets for boosting charge separation and photocatalytic CO₂ reduction. *Appl. Catal. B.* **2020**, *277*, 119230. [[CrossRef](#)]
85. Connor, B.A.; Leppert, L.; Smith, M.D.; Neaton, J.B.; Karunadasa, H.I. Layered halide double perovskites: Dimensional reduction of Cs₂AgBiBr₆. *J. Am. Chem. Soc.* **2018**, *140*, 5235–5240. [[CrossRef](#)] [[PubMed](#)]
86. Brandt, R.E.; Stevanović, V.; Ginley, D.S.; Buonassisi, T. Identifying defect-tolerant semiconductors with high minority-carrier lifetimes: Beyond hybrid lead halide perovskites. *MRS Commun.* **2015**, *5*, 265–275. [[CrossRef](#)]
87. Huang, S.; Shan, H.; Xuan, W.; Xu, W.; Hu, D.; Zhu, L.; Huang, C.; Sui, W.; Xiao, C.; Zhao, Y.; et al. High-Performance Humidity Sensor Based on CsPbBr₃ Nanocrystals for Noncontact Sensing of Hydromechanical Characteristics of Unsaturated Soil. *Phys. Status Solidi—Rapid Res. Lett.* **2022**, *16*, 2200017. [[CrossRef](#)]
88. Guo, J.; Hu, Q.; Lu, M.; Li, A.; Zhang, X.; Sheng, R.; Chen, P.; Zhang, Y.; Wu, J.; Fu, Y.; et al. Pb²⁺ doped CsCdBr₃ perovskite nanorods for pure-blue light-emitting diodes. *Chem. Eng. J.* **2022**, *427*, 131010. [[CrossRef](#)]
89. Chaiyawat, K.; Laosiritaworn, Y.; Jaroenjittichai, A.P. First-principles study on structural stability and reaction with H₂O and O₂ of vacancy-ordered double perovskite halides: Cs₂(Ti, Zr, Hf)X₆. *Results Phys.* **2021**, *25*, 104225.
90. Gundiah, G.; Brennan, K.; Yan, Z.; Samulon, E.C.; Wu, G.; Bizarri, G.A.; Derenzo, S.E.; Bourret-Courchesne, E.D. Structure and scintillation properties of Ce³⁺-activated Cs₂NaLaCl₆, Cs₃LaCl₆, Cs₂NaLaBr₆, Cs₃LaBr₆, Cs₂NaLaI₆ and Cs₃LaI₆. *J. Lumin.* **2014**, *149*, 374–384. [[CrossRef](#)]
91. Krishnamoorthy, T.; Ding, H.; Yan, C.; Leong, W.L.; Baikie, T.; Zhang, Z.; Sherburne, M.; Li, S.; Asta, M.; Mathews, N.; et al. Lead-free germanium iodide perovskite materials for photovoltaic applications. *J. Mater. Chem. A* **2015**, *3*, 23829. [[CrossRef](#)]
92. Ahmad, K. Bismuth Halide Perovskites for Photovoltaic Applications. In *Bismuth—Fundamentals and Optoelectronic Applications*; IntechOpen: London, UK, 2020.
93. Yu, B.-B.; Liao, M.; Yang, J.; Chen, W.; Zhu, Y.; Zhang, X.; Duan, T.; Yao, W.; Wei, S.-H.; He, Z. Alloy-induced phase transition and enhanced photovoltaic performance: The case of Cs₃Bi₂I_{9-x}Br_x perovskite solar cells. *J. Mater. Sci.* **2019**, *7*, 8818–8825. [[CrossRef](#)]
94. Cui, Z.; Wu, Y.; Zhang, S.; Fu, H.; Chen, G.; Lou, Z.; Liu, X.; Zhang, Q.; Wang, Z.; Zheng, Z.; et al. Insight into a strategy to improve charge carrier migration in lead-free bismuth-based halide perovskite for efficient selective oxidation of thioanisole under visible light. *Chem. Eng. J.* **2023**, *451*, 138927. [[CrossRef](#)]
95. Estrada-Pomares, J.; Ramos-Terrón, S.; Lasarte-Aragonés, G.; Lucena, R.; Cárdenas, S.; Rodríguez-Padrón, D.; Luque, R.; de Miguel, G. Mechanochemically designed bismuth-based halide perovskites for efficient photocatalytic oxidation of vanillyl alcohol. *J. Mater. Chem. A* **2022**, *10*, 11298–11305. [[CrossRef](#)]
96. Bresolin, B.-M.; Günemann, C.; Bahnemann, D.W.; Sillanpää, M. Pb-Free Cs₃Bi₂I₉ Perovskite as a Visible-Light-Active Photocatalyst for Organic Pollutant Degradation. *Nanomaterials* **2020**, *10*, 763. [[CrossRef](#)] [[PubMed](#)]
97. Miodyńska, M.; Mikolajczyk, A.; Mazierski, P.; Klimczuk, T.; Lisowski, W.; Trykowski, G.; Zaleska-Medynska, A. Lead-free bismuth-based perovskites coupled with g-C₃N₄: A machine learning based novel approach for visible light induced degradation of pollutants. *Appl. Surf. Sci.* **2022**, *588*, 152921. [[CrossRef](#)]
98. Bhosale, S.S.; Kharade, A.K.; Jokar, E.; Fathi, A.; Chang, S.-m.; Diau, E.W.-G. Mechanism of Photocatalytic CO₂ Reduction by Bismuth-Based Perovskite Nanocrystals at the Gas–Solid Interface. *J. Am. Chem. Soc.* **2019**, *141*, 20434–20442. [[CrossRef](#)] [[PubMed](#)]
99. Bresolin, B.-M.; Balayeva, N.O.; Granone, L.I.; Dillert, R.; Bahnemann, D.W.; Sillanpää, M. Anchoring lead-free halide Cs₃Bi₂I₉ perovskite on UV100–TiO₂ for enhanced photocatalytic performance. *Sol. Energy Mater. Sol. Cells* **2020**, *204*, 110214. [[CrossRef](#)]
100. Leng, M.; Yang, Y.; Zeng, K.; Chen, Z.; Tan, Z.; Li, S.; Li, J.; Xu, B.; Li, D.; Hautzinger, M.P.; et al. All-Inorganic Bismuth-Based Perovskite Quantum Dots with Bright Blue Photoluminescence and Excellent Stability. *Adv. Funct. Mater.* **2018**, *28*, 1704446. [[CrossRef](#)]
101. Xiaojia, Z.; Wei, Z.; Peng, W.; Hairen, T.; Saidaminov, M.I.; Shujie, T.; Ligao, C.; Yufei, P.; Jidong, L.; Wen-Hua, Z. Ultrasensitive and stable X-ray detection using zero-dimensional lead-free perovskites. *J. Energy Chem.* **2020**, *49*, 299–306.
102. Lehner, A.J.; Fabini, D.H.; Evans, H.A.; Hébert, C.-A.; Smock, S.R.; Hu, J.; Wang, H.; Zwanziger, J.W.; Chabiny, M.L.; Seshadri, R. Crystal and Electronic Structures of Complex Bismuth Iodides A₃Bi₂I₉ (A = K, Rb, Cs) Related to Perovskite: Aiding the Rational Design of Photovoltaics. *Chem. Mater.* **2015**, *27*, 7137–7148. [[CrossRef](#)]
103. Nair, S.; Bhorde, A.; Kulkarni, R.; Bade, B.; Punde, A.; Vairale, P.; Hase, Y.; Waghmare, A.; Waykar, R.; Deshpande, M.; et al. Synthesis and characterization of inorganic K₃Bi₂I₉ perovskite thin films for lead-free solution processed solar cells. *Mater. Today Proc.* **2021**, *32*, 684–689. [[CrossRef](#)]

104. Sheng, J.; He, Y.; Li, J.; Yuan, C.; Huang, H.; Wang, S.; Sun, Y.; Wang, Z.; Dong, F. Identification of Halogen-Associated Active Sites on Bismuth-Based Perovskite Quantum Dots for Efficient and Selective CO₂-to-CO Photoreduction. *ACS Nano* **2020**, *14*, 13103–13114. [[CrossRef](#)]
105. Jain, S.M.; Phuyal, D.; Davies, M.L.; Li, M.; Philippe, B.; De Castro, C.; Qiu, Z.; Kim, J.; Watson, T.; Tsoi, W.C.; et al. An effective approach of vapour assisted morphological tailoring for reducing metal defect sites in lead-free, (CH₃NH₃)₃Bi₂I₉ Bismuth-based perovskite solar cells for improved performance and long-term stability. *Nano Energy* **2018**, *49*, 614–624. [[CrossRef](#)]
106. Teo, S.H.; Ng, C.H.; Ng, Y.H.; Islam, A.; Hayase, S.; Taufiq-Yapa, Y.H. Resolve deep-rooted challenges of halide perovskite for sustainable energy development and environmental remediation. *Nano Energy* **2022**, *99*, 107401. [[CrossRef](#)]
107. Xiang, G.; Wu, Y.; Zhang, M.; Cheng, C.; Leng, J.; Ma, H. Dimension-Dependent Bandgap Narrowing and Metallization in Lead-Free Halide Perovskite Cs₃Bi₂X₉ (X = I, Br, and Cl) under High Pressure. *Nanomaterials* **2021**, *11*, 2712. [[CrossRef](#)] [[PubMed](#)]
108. Yang, K.; Wang, Y.; Shen, J.; Scott, S.M.; Riley, B.J.; Vienna, J.D.; Lian, J. Cs₃Bi₂I₉-hydroxyapatite composite waste forms for cesium and iodine immobilization. *J. Adv. Ceram.* **2022**, *11*, 712–728. [[CrossRef](#)]
109. Aristidou, N.; Eames, C.; Sanchez-Molina, I.; Bu, X.; Kosco, J.; Islam, M.S.; Haque, S.A. Fast oxygen diffusion and iodide defects mediate oxygen-induced degradation of perovskite solar cells. *Nature Commun.* **2017**, *8*, 15218. [[CrossRef](#)]
110. Aristidou, N.; Sanchez-Molina, I.; Chotchuangchutthaval, T.; Brown, M.; Martinez, L.; Rath, T.; Haque, S.A. The Role of Oxygen in the Degradation of Methylammonium Lead Trihalide Perovskite Photoactive Layers. *Angew. Chem.* **2015**, *54*, 8208–8212. [[CrossRef](#)]
111. Song, W.; Zhang, X.; Lammar, S.; Qiu, W.; Kuang, Y.; Ruttens, B.; D’Haen, J.; Vaesen, I.; Conard, T.; Abdurraheem, Y.; et al. Critical Role of Perovskite Film Stoichiometry in Determining Solar Cell Operational Stability: A Study on the Effects of Volatile A-Cation Additives. *ACS Appl. Mater. Interfaces* **2022**, *14*, 27922–27931. [[CrossRef](#)]
112. Fabian, D.M.; Ganose, A.M.; Ziller, J.W.; Scanlon, D.O.; Beard, M.C.; Ardo, S. Influence of One Specific Carbon–Carbon Bond on the Quality, Stability, and Photovoltaic Performance of Hybrid Organic–Inorganic Bismuth Iodide Materials. *ACS Appl. Energy Mater.* **2019**, *2*, 1579–1587. [[CrossRef](#)]
113. Trifiletti, V.; Luong, S.; Tseberlidis, G.; Riva, S.; Galindez, E.S.S.; Gillin, W.P.; Binetti, S.; Fenwick, O. Two-Step Synthesis of Bismuth-Based Hybrid Halide Perovskite Thin-Films. *Materials* **2021**, *14*, 7827. [[CrossRef](#)]
114. Leng, M.; Yang, Y.; Chen, Z.; Gao, W.; Zhang, J.; Niu, G.; Li, D.; Song, H.; Zhang, J.; Jin, S.; et al. Surface Passivation of Bismuth-Based Perovskite Variant Quantum Dots to Achieve Efficient Blue Emission. *Nano Lett.* **2018**, *18*, 6076–6083. [[CrossRef](#)]
115. Mali, S.S.; Kim, H.; Kim, D.-H.; Hong, C.K. Anti-Solvent Assisted Crystallization Processed Methylammonium Bismuth Iodide Cuboids towards Highly Stable Lead-Free Perovskite Solar Cells. *Energy Environ. Sci.* **2017**, *2*, 1578–1585. [[CrossRef](#)]
116. Liu, Z.; Chen, M.; Wan, L.; Liu, Y.; Wang, Y.; Gan, Y.; Guo, Z.; Eder, D.; Wang, S. Anti-solvent spin-coating for improving morphology of lead-free (CH₃NH₃)₃Bi₂I₉ perovskite films. *SN Appl. Sci.* **2019**, *1*, 706. [[CrossRef](#)]
117. Konstantakou, M.; Perganti, D.; Falaras, P.; Stergiopoulos, T. Anti-Solvent Crystallization Strategies for Highly Efficient Perovskite Solar Cells. *Crystals* **2017**, *7*, 291. [[CrossRef](#)]
118. Corsini, F.; Griffini, G. Recent progress in encapsulation strategies to enhance the stability of organometal halide perovskite solar cells. *J Phys Energy* **2020**, *2*, 031002. [[CrossRef](#)]
119. Li, Q.; Song, T.; Zhang, Y.; Wang, Q.; Yang, Y. Boosting Photocatalytic Activity and Stability of Lead-Free Cs₃Bi₂Br₉ Perovskite Nanocrystals via In Situ Growth on Monolayer 2D Ti₃C₂T_x MXene for C–H Bond Oxidation. *ACS Appl. Mater. Interfaces* **2021**, *13*, 27323–27333. [[CrossRef](#)]
120. Sun, Q.; Ye, W.; Wei, J.; Li, L.; Wang, J.; He, J.-H.; Lu, J.-M. Lead-free perovskite Cs₃Bi₂Br₉ heterojunctions for highly efficient and selective photocatalysis under mild conditions. *J. Alloys Compd.* **2022**, *893*, 162326. [[CrossRef](#)]
121. Bresolin, B.-M.; Sgarbossa, P.; Bahnemann, D.W.; Sillanpää, M. Cs₃Bi₂I₉/g-C₃N₄ as a new binary photocatalyst for efficient visible-light photocatalytic processes. *Sep. Purif. Technol.* **2020**, *251*, 117320. [[CrossRef](#)]
122. Guo, Y.; Liu, G.; Li, Z.; Lou, Y.; Chen, J.; Zhao, Y. Stable Lead-Free (CH₃NH₃)₃Bi₂I₉ Perovskite for Photocatalytic Hydrogen Generation. *ACS Sustain. Chem. Eng.* **2019**, *7*, 15080–15085. [[CrossRef](#)]
123. García-Fernández, A.; Juárez-Perez, E.J.; Castro-García, S.; Sánchez-Andújar, M.; Ono, L.K.; Jiang, Y.; Qi, Y. Benchmarking Chemical Stability of Arbitrarily Mixed 3D Hybrid Halide Perovskites for Solar Cell Applications. *Small* **2018**, *2*, 1800242. [[CrossRef](#)]
124. Wu, D.; Zhao, X.; Huang, Y.; Lai, J.; Yang, J.; Tian, C.; Hea, P.; Huang, Q.; Tang, X. Synthesis and CO₂ Photoreduction of Lead-Free Cesium Bismuth Halide Perovskite Nanocrystals. *J. Phys. Chem. C* **2021**, *25*, 18328–18333. [[CrossRef](#)]
125. Ghosh, S.; Shankar, H.; Kar, P. Recent developments of lead-free halide double perovskites: A new superstar in the optoelectronic field. *Mater. Adv.* **2022**, *3*, 3742. [[CrossRef](#)]
126. Liu, Z.; Yang, H.; Wang, J.; Yuan, Y.; Hills-Kimball, K.; Cai, T.; Wang, P.; Tang, A.; Chen, O. Synthesis of Lead-Free Cs₂AgBiX₆ (X = Cl, Br, I) Double Perovskite Nanoplatelets and Their Application in CO₂ Photocatalytic Reduction. *Nano Lett.* **2021**, *21*, 1620–1627. [[CrossRef](#)] [[PubMed](#)]
127. Sun, Q.-M.; Xu, J.-J.; Tao, F.-F.; Ye, W.; Zhou, C.; He, J.-H.; Lu, J.-M. Boosted Inner Surface Charge Transfer in Perovskite Nanodots@Mesoporous Titania Frameworks for Efficient and Selective Photocatalytic CO₂ Reduction to Methane. *Angew. Chem.* **2022**, *134*, e202200872.
128. Zhou, L.; Xu, Y.-F.; Chen, B.-X.; Kuang, D.-B.; Su, C.-Y. Synthesis and Photocatalytic Application of Stable Lead-Free Cs₂AgBiBr₆ Perovskite Nanocrystals. *Small* **2018**, *14*, 1703762. [[CrossRef](#)] [[PubMed](#)]

129. Wu, D.; Zhao, X.; Huang, Y.; Lai, J.; Li, H.; Yang, J.; Tian, C.; He, P.; Huang, Q.; Tang, X. Lead-Free Perovskite Cs₂AgBiX₆ Nanocrystals with a Band Gap Funnel Structure for Photocatalytic CO₂ Reduction under Visible Light. *Chem. Mater.* **2021**, *33*, 4971–4976. [[CrossRef](#)]
130. Wang, Y.; Huang, H.; Zhang, Z.; Wang, C.; Yang, Y.; Li, Q.; Xu, D. Lead-free perovskite Cs₂AgBiBr₆@g-C₃N₄ Z-scheme system for improving CH₄ production in photocatalytic CO₂ reduction. *Appl. Catal. B.* **2021**, *282*, 119570. [[CrossRef](#)]
131. Zhang, Z.; Wang, B.; Zhao, H.-B.; Liao, J.-F.; Zhou, Z.C.; Liu, T.; He, B.; Wei, Q.; Chen, S.; Chen, H.-Y.; et al. Self-assembled lead-free double perovskite-MXene heterostructure with efficient charge separation for photocatalytic CO₂ reduction. *Appl. Catal. B.* **2022**, *312*, 121358. [[CrossRef](#)]
132. Luévano-Hipólito, E.; Garay-Rodríguez, L.F.; Torres-Martínez, L.M. Photocatalytic heterostructured materials for air decontamination and solar fuels production. In *Handbook of Greener Synthesis of Nanomaterials and Compounds*; Elsevier: Amsterdam, The Netherlands, 2021; Volume 2, pp. 593–636.
133. Dou, Y.; Zhou, A.; Yao, Y.; Lim, S.Y.; Li, J.-R.; Zhang, W. Suppressing hydrogen evolution for high selective CO₂ reduction through surface-reconstructed heterojunction photocatalyst. *Appl. Catal. B.* **2021**, *286*, 119876. [[CrossRef](#)]
134. Luévano-Hipólito, E.; Torres-Martínez, L.M. Earth-abundant ZnS/ZnO/CuFeS₂ films for air purification and solar fuels production. *Mater. Sci. Semicond. Process.* **2021**, *134*, 106029. [[CrossRef](#)]
135. Mu, Q.; Zhu, W.; Li, X.; Zhang, C.; Su, Y.; Lian, Y.; Qi, P.; Deng, Z.; Zhang, D.; Wang, S.; et al. Electrostatic charge transfer for boosting the photocatalytic CO₂ reduction on metal centers of 2D MOF/rGO heterostructure. *Appl. Catal. B.* **2020**, *262*, 118144. [[CrossRef](#)]
136. Li, D.; Zhu, B.; Sun, Z.; Liu, Q.; Wang, L.; Tang, H. Construction of UiO-66/Bi₄O₅Br₂ Type-II Heterojunction to Boost Charge Transfer for Promoting Photocatalytic CO₂ Reduction Performance. *Front. Chem.* **2021**, *9*, 804204. [[CrossRef](#)] [[PubMed](#)]
137. Liu, Z.-L.; Liu, R.-R.; Mu, Y.-F.; Feng, Y.-X.; Dong, G.-X.; Zhang, M.; Lu, T.-B. In Situ Construction of Lead-Free Perovskite Direct Z-Scheme Heterojunction Cs₃Bi₂I₉/Bi₂WO₆ for Efficient Photocatalysis of CO₂ Reduction. *Sol. RRL* **2021**, *5*, 2000691. [[CrossRef](#)]
138. Zhao, B.; Pan, Y.-X.; Liu, C.-J. The promotion effect of CeO₂ on CO₂ adsorption and hydrogenation over Ga₂O₃. *Catal. Today* **2012**, *194*, 60–64. [[CrossRef](#)]
139. Feng, Y.-X.; Dong, G.-X.; Su, K.; Liu, Z.-L.; Zhang, W.; Zhang, M.; Lu, T.-B. Self-template-oriented synthesis of lead-free perovskite Cs₃Bi₂I₉ nanosheets for boosting photocatalysis of CO₂ reduction over Z-scheme heterojunction Cs₃Bi₂I₉/CeO₂. *J. Energy Chem.* **2022**, *69*, 348–355. [[CrossRef](#)]
140. Zhang, Z.; Wang, M.; Chi, Z.; Li, W.; Yu, H.; Yang, N.; Yu, H. Internal electric field engineering step-scheme-based heterojunction using lead-free Cs₃Bi₂Br₉ perovskite-modified In₄SnS₈ for selective photocatalytic CO₂ reduction to CO. *Appl. Catal. B.* **2022**, *313*, 121426. [[CrossRef](#)]
141. Otero-Martínez, C.; Fiuza-Maneiro, N.; Polavarapu, L. Enhancing the Intrinsic and Extrinsic Stability of Halide Perovskite Nanocrystals for Efficient and Durable Optoelectronics. *ACS Appl. Mater. Interfaces* **2022**, *14*, 34291–34302. [[CrossRef](#)]
142. Cui, Z.; Wang, P.; Wu, Y.; Liu, X.; Chen, G.; Gao, P.; Zhang, Q.; Wang, Z.; Zheng, Z.; Cheng, H.; et al. Space-confined growth of lead-free halide perovskite Cs₃Bi₂Br₉ in MCM-41 molecular sieve as an efficient photocatalyst for CO₂ reduction at the gas–solid condition under visible light. *Appl. Catal. B.* **2022**, *310*, 121375. [[CrossRef](#)]